

# Electrospun Fe<sub>2</sub>O<sub>3</sub> Entrenched SiO<sub>2</sub> Supported N and S Dual Incorporated TiO<sub>2</sub> Nanofibers Derived from Mixed Polymeric Template/Surfactant: Enriched Mesoporosity within Nanofibers, Effective Charge Separation, and Visible Light Photocatalysis Activity

Amaresh C. Pradhan<sup>\*,†,‡</sup> and Tamer Uyar<sup>\*,†,‡,§</sup>

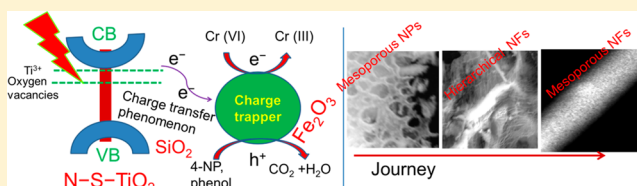
<sup>†</sup>Institute of Materials Science & Nanotechnology, Bilkent University, Ankara, 06800, Turkey

<sup>‡</sup>Department of Fiber Science and Apparel Design, College of Human Ecology, Cornell University, Ithaca, New York 14853, United States

## S Supporting Information

**ABSTRACT:** The  $\alpha$ -Fe<sub>2</sub>O<sub>3</sub> promoted and SiO<sub>2</sub> supported N and S dual incorporated TiO<sub>2</sub> nanofibers (FeSiNST NFs) along with neat oxide NFs have been synthesized by electrospinning via sol–gel. The keen approach is that mixed polyvinylpyrrolidone (PVP) as template and cetyltrimethylammonium bromide (CTAB) as surfactant are responsible for the creation of mesoporosity within NFs.

The photoluminescence (PL) spectrum and UV–visible diffuse reflectance spectroscopic (DRS) result revealed the role of  $\alpha$ -Fe<sub>2</sub>O<sub>3</sub> as catalytic promoter in FeSiNST NFs by suppressing electron–hole ( $e^-$ – $h^+$ ) recombination, red shifting, and oxygen vacancies ( $O_{vs}$ ). The design of FeSiNST NFs by combining with SiO<sub>2</sub> as catalytic support and N and S as visible light absorbers in TiO<sub>2</sub>, beautifies the present study. The high photocurrent (3.2 mA/cm<sup>2</sup>), high  $E_{fb}$  value (–1.0 V), and low  $R_{ct}$  value ( $\sim$ 74  $\Omega$ ) support the enhanced photocatalysis (photoreduction and photodegradation) by FeSiNST in visible light. Charge transfer phenomena,  $O_{vs}$ , mesoporosity, and separation of  $e^-$ – $h^+$  are the vital factors for an effective photocatalysis achievement.



## 1. INTRODUCTION

The fabrication and nanodesign of photocatalysts with semiconductor property have attracted momentous attention due to their superior performance in pollutant remediation.<sup>1,2</sup> Phenol, 4-nitrophenol (4-NP), and heavy metal ions such as Cr(IV) are noxious pollutants which are produced from the chemical industry.<sup>3–5</sup> These above-mentioned pollutants have detrimental influence toward whole ecosystem because they are poisonous and carcinogenic.<sup>6</sup> Researchers have utilized various nanodesigned materials such as nanorods, nanoparticles, nanotubes, nanowires, and nanoflowers for photocatalytic removal of pollutants and toxic elements. This is because nanodesigned materials have unique optical properties, such as sharp light-harvesting property and wide surface to volume ratio, and distinctive textural properties, such as surface area ( $S_A$ ).<sup>7–10</sup> Larger charge momentum, grain limits, swift ion distribution, and smart light absorption are the key properties which increase the great deal of attention in one-dimensional (1D) nanodesigned materials.<sup>11,12</sup> Metal oxide nanofibers (NFs) having 1D structure fabricated by electrospinning process have remarkable features such as mesoporosity, great surface area to volume ratio, and proficient catalytic support.<sup>2,13,14</sup> Electrospun anatase ( $\sim$ 3.2 eV) TiO<sub>2</sub> NFs, an example of metal oxide NFs, have been used as a photocatalyst and sensor. This is due to their semiconductor property, long-

range photoresponse in the UV region, nontoxicity, and cost effectiveness.<sup>15,16</sup> It has been noted that TiO<sub>2</sub> NFs fabricated by electrospinning are more competent compared to TiO<sub>2</sub>. Facile  $e^-$ – $h^+$  momentum within the grain is an important factor for  $e^-$  and  $h^+$  separation.<sup>17</sup> Hence, researchers are enthusiastic in their research of designing and modifying TiO<sub>2</sub> NFs materials toward visible light action. Visible light response photocatalysts have many advantages over UV light. These are including costeffectiveness, ease of handling, green approach, and reaction fitness.

The design and development of anatase TiO<sub>2</sub> NFs is essential in order to make visible light active photocatalysts toward photodegradation of 4-NP and phenol, and photoreduction of Cr(VI). Hence, the following strategic modifications will fulfill our target. These are (i) creation of mesoporosity within TiO<sub>2</sub> NFs as base photocatalyst, (ii) N and S dual incorporation as a visible light absorber, (iii) modification of Fe<sub>2</sub>O<sub>3</sub> as a promoter, (iv) introduction of SiO<sub>2</sub> as a mesoporous catalytic support, and (v) mixing all the above ingredients to form a stable mesoporous FeSiNST NFs

**Received:** February 19, 2019

**Revised:** May 27, 2019

**Accepted:** June 24, 2019

**Published:** June 24, 2019

photocatalyst. Mesoporosity and NFs morphology have great impact in photocatalysis applications.<sup>13,14</sup> This is because NFs morphology enables easy movement of the  $e^-$  and  $h^+$  on the catalyst surface, whereas mesoporosity enhances the  $S_A$  and surface reactive sites. Moreover, mesoporosity and NFs enhance the light absorption property and charge transport ability. Textural properties such as mesoporosity, NFs morphology, and  $S_A$  have great importance for the construction of a photocatalyst. The electrospinning route may provide a better option to achieve the mesoporosity,  $S_A$ , and NFs morphology within  $TiO_2$  ( $TiO_2$  NFs). The electrospinning route provides a better platform to generate NFs and porous morphology by including an apposite template, surfactant, and other additives.<sup>18,19</sup> Hence the design and modification of the  $TiO_2$  toward mesoporosity within NFs morphology by applying a suitable mixture of template (polyvinylpyrrolidone, PVP) and surfactant (cetyltrimethylammonium bromide, CTAB) will be the novel approach. It has been studied that a mixture of N and S into the  $TiO_2$  performs a bathochromic property.<sup>20</sup> This is the main reason that researchers are interested to incorporate N and S into metal oxides for making visible light response photocatalysts. Hence, N and S dual incorporation will make the long-range light absorption property, i.e., red shifting which is due to induction of N 2p and S 2p states in the lattice of the metal oxide.<sup>20,21</sup> Thus, N and S dual incorporation into a single metal oxide semiconductor like  $TiO_2$  will act as a visible light response photocatalyst. In the photocatalysis process the quick  $e^-h^+$  recombination is an adverse situation which inhibits the progress of photocatalysis reaction. Hence, in order to make an efficient photocatalyst, a suitable charge-deficient center is essential to suppress the  $e^-h^+$  recombination.  $\alpha$ -Iron oxide ( $\alpha-Fe_2O_3$ ) has attracted notable attention due to its stability, cost effectiveness, nonpoisonous property, environmental sociability, suitable band gap range (2.0–2.2 eV), and positive valence band edge potential. The advantages regarding the introduction of  $\alpha-Fe_2O_3$  ( $Fe^{3+}$ ) within N–S– $TiO_2$  (NST) are as follows:

- (i) It possesses  $3d^5$  (half-filled) electronic configuration.
- (ii) The ionic radius of  $Fe^{3+}$  (0.064 nm) is nearly similar to the ionic radius of  $Ti^{4+}$ , 0.068 nm,<sup>22</sup> and the resulting  $Fe^{3+}$  may have the ability to combine into the  $TiO_2$  structure through a substitutional and interstitial approach.
- (iii)  $Fe^{3+}$  may perform as a charge trapping center within the NST lattice which is because of the charge transfer transition and d–d transition. This process may approve the suppressing of  $e^-h^+$  recombination and encompassing the photocatalysis activity.
- (iv) Combining of metal oxide ( $\alpha-Fe_2O_3$ ) as a promoter in the form of  $Fe^{3+}$  in NST weakens the bonding of adjacent oxygen atoms. This will result in the creation of  $O_{vs}$  due to the release of oxygen atoms from the lattice.<sup>22</sup>

Hence, adaptation of  $\alpha-Fe_2O_3$  as a catalytic promoter within the NST NFs may achieve our proficient photocatalysis strategy and decrease the  $e^-h^+$  recombination. In order to increase/distribute the catalyst reactive sites, an appropriate catalytic support is required. Mesoporous silica based materials have been used as catalyst supports in many photocatalysis applications because of high textural properties such as large  $S_A$ , wide  $P_V$ , and narrow pore size ( $P_S$ ).<sup>23,24</sup> Hence, amendment of  $SiO_2$  into the framework of NST lattice will offer the vital catalytic support to the semiconductor  $\alpha-Fe_2O_3$  and  $TiO_2$ . Thus, nanodesign of  $\alpha-Fe_2O_3$  as promoter and  $SiO_2$

as support within NST ( $FeSiNST$ ) having a mesoporosity within the NFs morphology could be able to enhance visible light absorption and diminish the recombination of  $e^-h^+$  which may lead to an efficient Cr(VI) photoreduction, and 4-NP and phenol photodegradation.

Here, we describe the synthesis and design of mesoporous photocatalysts such as  $TiO_2$  NFs,  $SiO_2$  NFs, NST NFs, and  $FeSiNST$  NFs by the electrospinning via sol–gel route. Mixed PVP and CTAB have taken the important role in the synthesis of the aforesaid NFs samples. The mechanistic pathway for the formation of mesoporosity within NFs has also been explored. The mechanism of the photoreduction of Cr(VI) and photodegradation of 4-NP and phenol has been included. The role of the semiconductor  $\alpha-Fe_2O_3$  as a charge trapping center/promoter, N and S as visible light absorber,  $TiO_2$  as base semiconductor photocatalyst, and  $SiO_2$  as catalyst support is enhancing the photocatalysis activity in the  $FeSiNST$  NFs by separation of  $e^-$  and  $h^+$ . The synergetic action of N, S,  $TiO_2$ ,  $\alpha-Fe_2O_3$ , and  $SiO_2$  in the mesoporous  $FeSiNST$  NFs displays the maximum photocatalysis performance over neat NFs. The mesoporosity within NFs, high  $S_A$ , optical properties, and charge transfer phenomena have key roles for an enhanced photocatalysis performance.

## 2. EXPERIMENTAL SECTION

**2.1. Materials.** The chemicals involved in the research were of analytical quality. These were used directly in the reaction without purification. Titanium isopropoxide ( $Ti(iPr)_4$ ), tetraethyl orthosilicate (TEOS,  $Si(OC_2H_5)_4$ ), PVP ( $M_w = 130000$  g/mol), and potassium iodide (KI) were from Aldrich, whereas iron chloride ( $Fe(III)Cl \cdot 6H_2O$ ) was from Sigma-Aldrich. Thiourea ( $CH_4N_2S$ ), CTAB, 4-nitrophenol (4-NP), phenol, potassium dichromate ( $K_2Cr_2O_7$ ), and *p*-benzoquinone used were from Alfa Aesar.

**2.2. Fabrication of Mesoporous  $TiO_2$  and  $SiO_2$  NFs by Electrospinning via Sol–Gel.** The electrospinning via sol–gel route was introduced to synthesize  $TiO_2$  NFs and  $SiO_2$  NFs. For  $TiO_2$  NFs synthesis, 1 mL of titanium isopropoxide was added in 8 mL of isopropanol in a beaker. Then, PVP (1.0 g) was inserted and stirred well for 2 h. Afterward, 0.15 g of CTAB mixed with 3 mL of  $H_2O$  was added into the above solution. Lastly, acetic acid (2.5 mL) was mixed into the solution and stirred for 12 h. The gel was filled into a plastic syringe (3 mL) with a needle diameter of 0.4 mm and connected to a syringe pump (KDS101, KD Scientific, USA). The gel rate of flow was sustained at 0.8 mL/h with a supply of an 11.5 kV electric field. The voltage was delivered by Spellman, USA. Aluminum foil was connected in the electric field to collect the sample. The temperature and humidity were maintained at 23 °C and 18%, respectively. The synthesized  $TiO_2$ /PVP/CTAB mixed NFs were calcined at 450 °C for 5 h, and finally mesoporous  $TiO_2$  NFs were produced. The mesoporous  $SiO_2$  NFs were prepared with exactly the same method as for  $TiO_2$  NFs, only by adding 1 mL of TEOS as the source of silica. The mesoporous  $SiO_2$  NFs were produced after removal of PVP and CTAB from  $SiO_2$ /PVP/CTAB mixed NFs at the calcination temperature 450 °C for 5 h.

**2.3. Electrospinning via Sol–Gel Fabrication of Mesoporous NST NFs,  $FeSiNST$  NFs,  $FeSiNST$  HNFs, and Electrospinning  $FeSiNST$  MNPs.** In the beginning, 1.5 g of PVP was mixed with 12 mL of isopropanol in a beaker. In a separate beaker 0.15 g of CTAB was mixed in 3 mL of  $H_2O$ . Both solutions were mixed well along with 0.5 g of thiourea

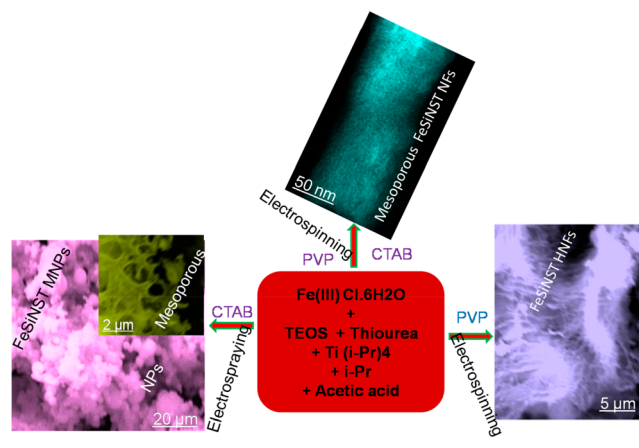
introduced as a source of N and S. Afterward, titanium isopropoxide (2 mL) was mixed in and stirred in order to get a sol. Lastly, acetic acid (2 mL) was mixed as a solution stabilizer to maintain the proper viscosity for the electrospinning via sol–gel process. The resultant mixture was stirred for 12 h. The mild gray colored gel solution was set for exactly the same electrospinning via sol–gel procedure as for the TiO<sub>2</sub> NFs. The mild gray color is because of the presence of S. Moreover, the mesoporous N and S dual incorporated TiO<sub>2</sub> NFs (NST NFs) were formed after calcination (450 °C, 5 h).

Similarly, mesoporous  $\alpha$ -Fe<sub>2</sub>O<sub>3</sub> promoted and SiO<sub>2</sub> supported with N and S mixed TiO<sub>2</sub> nanofibers (mesoporous FeSiNST NFs) were fabricated by a three-pot system. In the first pot, 1.5 g of PVP was mixed well in 12 mL of isopropanol. Subsequently, CTAB solution (0.15 g of CTAB mixed with 3 mL of H<sub>2</sub>O) was added into the above solution. Then, 0.5 g of thiourea and titanium isopropoxide (2 mL) was mixed. Next, acetic acid (3.5 mL) was added and stirred for getting a gray sol. This proves that N and S were incorporated into the Ti–O–Ti framework. In the second pot, 0.15 g of CTAB was mixed in H<sub>2</sub>O (5 mL) with continuous stirring. TEOS (0.5 mL) was added and stirred for 1 h. In the third pot, 0.6 g of Fe(III)Cl<sub>6</sub>H<sub>2</sub>O was added to 4 mL of isopropanol and stirred for 2 h. All of the three-pot reaction substances were mixed and stirred for 6 h to get a gel. The final gel filled a plastic syringe (3 mL) and followed the electrospinning process. The syringe pump with a flow rate of 0.5 mL/h was set up to regulate the gel flow. A fixed 15 kV (Spellman) was applied to continue the power supply. Finally, mesoporous FeSiNST NFs were formed by calcination at 450 °C for 5 h. The weights of Ti, Fe, Si, S, and N present in the FeSiNST NFs are 0.540, 0.142, 0.074, 0.053, and 0.038 g, respectively.

The FeSiNST hierarchical nanofibers were designated as FeSiNST HNFs. The synthesis procedure was like that of mesoporous FeSiNST NFs. Here the only difference was that PVP was taken as a template instead of mixed PVP and CTAB (template/surfactant). The material was calcined at 450 °C for 5 h and formed FeSiNST HNFs. The mesoporous FeSiNST nanoparticles (FeSiNST MNPs) were fabricated by an electrospaying process. The CTAB is used as a surfactant instead of mixed PVP and CTAB. The other precursors were similar to those in the synthesis of mesoporous FeSiNST NFs, but the difference was the electrospaying process. Finally, FeSiNST MNPs were formed after calcination at 450 °C in 5 h. Scheme 1 depicts the scanning electron microscopy (SEM)/scanning transmission electron microscopy (STEM) images of the FeSiNST MNPs, FeSiNST HNFs and mesoporous FeSiNST NFs by taking CTAB as surfactant, PVP as template, and PVP and CTAB as mixed template/surfactant, respectively. The creation of mesoporosity within NFs (FeSiNST NFs) is because of the mixture of PVP and CTAB as template/surfactant. But neat PVP and CTAB had important roles for the fabrication of FeSiNST HNFs and FeSiNST MNPs, respectively.

**2.4. Characterization.** The textural properties such as  $S_A$ , pore size ( $P_s$ ), and pore volume ( $P_v$ ) of the NFs were calculated from N<sub>2</sub> adsorption–desorption method at –196 °C (liquid N<sub>2</sub>). The experiment was done with a Quantachrome Instrument Autosorb (iQ2). A PANalytical X'Pert Pro multi-purpose X-ray diffractometer (XRD) was analyzed to check the crystal arrangement and phase of the NFs photocatalysts. The XRD of the sample was measured in the range  $2\theta = 10$ – $80^\circ$  with Cu K $\alpha$  (1.5418 Å) radiation. Field emission scanning

**Scheme 1.** Electrospayed Mesoporous FeSiNST MNPs (Surfactant, CTAB Only), Electrospun FeSiNST HNFs (Template, PVP Only), and Mesoporous FeSiNST NFs (Template/Surfactant, PVP/CTAB Mixture) Obtained after Calcination at 450 °C for 5 h



electron microscopy (FE-SEM) was analyzed with a Quanta 200 FEG, FEI, to check the morphology of the surface. A Tecnai G2 F30, FEI (high resolution transmission electron microscopy; HR-TEM) was employed to analyze the morphology and selected area electron diffraction (SAED) of the NFs. STEM with energy-dispersive X-ray spectroscopy (STEM-EDX) was applied to study the composition of the metal/elements in the form of oxides within the NFs. A Varian Cary 100, a UV–visible spectrophotometer, was used to record the absorption spectra of the synthesized materials. A Cary 500 was used to measure the UV–vis–near-infrared (NIR) diffuse reflectance spectroscopy (DRS). An FL-1057 TCSPC was used to analyze photoluminescence (PL) spectra. The spectra were measured with an excitation wavelength at 390 nm. A Thermo K-Alpha monochromated X-ray photoelectron spectrometer (XPS) was utilized to calculate the binding energy (BE) through XPS spectra with the excitation energy  $h\nu = 1484.6$  eV. The BEs of the NFs materials were plotted by using carbon (BE = 284.8 eV) as reference.

**2.5. Photocatalysis Activity in Visible Light.** The photocatalysis process, i.e., photoreduction of Cr(VI), progressed by utilizing 10 mL of K<sub>2</sub>Cr<sub>2</sub>O<sub>7</sub> (40 mg·L<sup>–1</sup>) solution, catalyst dose (1 mg·mL<sup>–1</sup>) at pH 4 within 80 min. Before photoreduction, the reaction solution with photocatalysts was stirred for 35 min in order to achieve equilibrium. A Mettler Toledo pH meter was used to measure the pH. Proper concentrations of nitric acid and NH<sub>3</sub> were mixed dropwise to adjust the pH of the solution. The suspension was set in a reactor (Osram, sunlight simulation) and exposed in visible light with a power of 300 W. After reaction, the catalyst was separated by filtration. The resultant product was inspected by a UV–vis spectrophotometer with a 350 nm absorption band.

Phenol and 4-NP photodegradation was examined by involving 30 mg·L<sup>–1</sup> concentrations of each pollutant. Both (phenol and 4-NP) solutions with presently synthesized NFs photocatalysts were stirred (40 min) individually to get equilibrium. The reaction proceeded by taking 10 mL of phenol and 4-NP separately with 1 mg·mL<sup>–1</sup> photocatalyst dose at pH 6 during 100 min. The pH analyzer, light source, and UV–vis spectrophotometer were used in the photodegradation

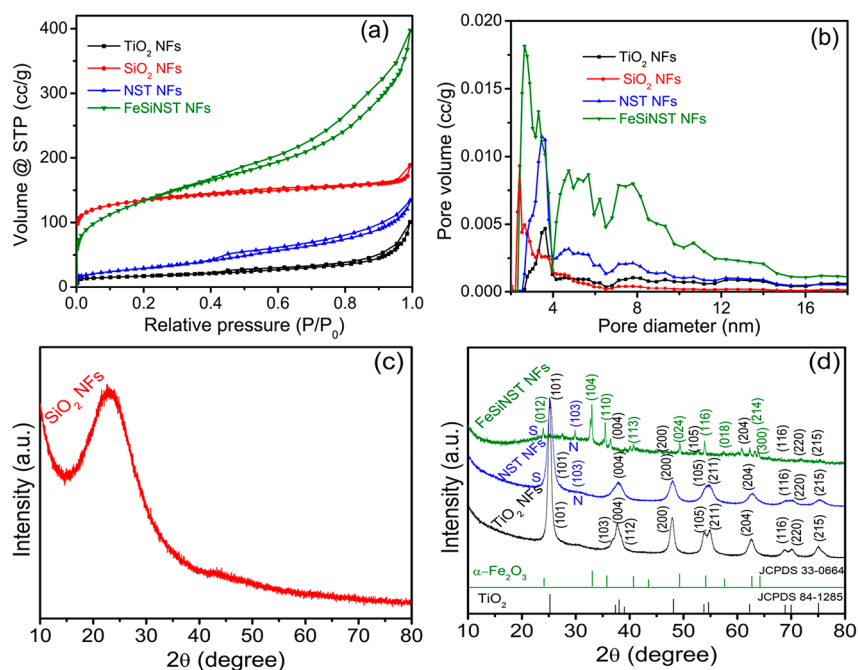


**Figure 1.** (a)  $N_2$  sorption isotherm, (b) pore size ( $P_s$ ), and (c) XRD pattern of mesoporous  $SiO_2$  NFs. (d) XRD patterns of  $TiO_2$  NFs, NST NFs, and FeSiNST NFs.

process, similar to the photoreduction of Cr(VI). Finally, the maximum absorbances of phenol (210 nm) and 4-NP (400 nm) were measured. The recyclability study of Cr(VI) reduction and 4-NP degradation by mesoporous FeSiNST NFs was carried out up to the fourth run in the optimum reaction condition. After the finish of each run, the mesoporous FeSiNST NFs material was calcined at 450 °C in 5 h in order to remove impurity and make reborn the mesoporosity.

**2.6. Trapping of Active Species.** The trapping reaction proceeded by adding different scavengers in the reaction media in the presence of FeSiNST NFs, which gives an idea about active species involved in reaction. In photocatalysis (photoreduction and photodegradation) reaction, 0.1 mmol of different scavengers such as KI, isopropyl alcohol (IPA), *p*-benzoquinone (BQ), and dimethyl sulfoxide (DMSO) was used to check the involvement of  $h^+$ ,  $\cdot OH$ ,  $O_2^{\cdot-}$ , and  $e^-$ , respectively. The trapping reaction situation is like the photoreduction of Cr(VI), and the photodegradation of 4-NP and phenol. The scavengers were mixed in reaction solution before the photocatalysis process.

**2.7. Photoelectrochemical Study.** The photoelectrochemical measurements were carried out by using platinum wire, Ag/AgCl electrode, and prepared electrode as the counter electrode, reference electrode, and working electrode, respectively. Electrodes were immersed in 0.1 M  $Na_2SO_4$  solution.  $N_2$  gas was used to saturate the electrolyte before electrochemical measurements. For photoelectrochemical measurement, an Ivum multichannel potentiostat with light irradiation ( $\lambda = 400$  nm) was used. Irradiation was executed by using a 300 W Xe lamp with a 400 nm cutoff filter.

### 3. RESULTS AND DISCUSSION

**3.1.  $N_2$  Adsorption–Desorption and XRD.** Figure 1a,b depicts the  $N_2$  adsorption–desorption isotherms and the  $P_s$  distributions of NFs. All NFs photocatalysts show type IV

isotherms having H1 and H3 hysteresis (Figure 1a). This type of hysteresis is the indication of mesoporosity.<sup>25</sup> The hysteresis loops of all NFs begin with  $P/P_0$  (relative pressure) of 0.1–0.5. This is due to the presence of narrow mesopores, i.e., intraparticle mesoporosity or “framework porosity”. The creation of mesoporosity within NFs is because of the removal of CTAB as surfactant at an optimal heat treatment at 450 °C in 5 h. Figure 1b describes the  $P_s$  (2–5 nm) of the NFs materials, and the ensuing mesoporous nature of NFs. The textural properties such as  $S_A$ ,  $P_s$ , and  $P_V$  of the NFs are shown in the Supporting Information (Table S1). Amazingly, the larger  $S_A$  values of  $TiO_2$  NFs,  $SiO_2$  NFs, NST NFs, and FeSiNST NFs, which are 50, 505, 110, and 300  $m^2/g$ , respectively, are calculated. Hence, high  $S_A$  values of NFs photocatalysts will offer more active spots for contact with Cr(VI), and 4-NP and phenol. The greater  $S_A$  of  $SiO_2$  NFs (505  $m^2/g$ ) than those of other synthesized NFs is a signpost of the involvement of  $SiO_2$  in FeSiNST NFs. The presence of  $SiO_2$  in FeSiNST NFs aids the enhancement of the  $S_A$  of the FeSiNST NFs (300  $m^2/g$ ). This is the vibrant reason to combine  $SiO_2$  in FeSiNST NFs as a support. The  $P_s$  values of the entire NFs samples belong to the mesoporous range (Table S1). All NFs samples possess wide  $P_V$ , indicating large  $S_A$  (Supporting Information). Hence, the  $N_2$  sorption isotherm provides clear information about the creation of mesoporosity and textural properties within the NFs.

Figure 1c displays the XRD pattern of the  $SiO_2$  NFs. The peak at  $2\theta = 22.6^\circ$  is assigned to the amorphous  $SiO_2$ .<sup>26</sup> XRD patterns of  $TiO_2$  NFs, NST NFs, FeSiNST NFs are exposed in Figure 1d. In the case of mesoporous  $TiO_2$  NFs, the peaks at 25.1, 36.9, 37.6, 38.5, 48.8, 53.8, 54.8, 62.7, 68.6, 70.1, and  $75^\circ$  matching with the planes (101), (103), (004), (112), (200), (105), (211), (204), (116), (220), and (215) because of the anatase  $TiO_2$  [JCPDS no. 84-1285]. For mesoporous NST NFs, the Bragg reflection angles correspond with the crystal planes of anatase  $TiO_2$ , including N (30.1°) for the (103)

plane and S at an angle of  $23^\circ$ .<sup>13,26</sup> The less intense peak of N and S in the respective material is because of the least quantity of N and S (dopant). The existence of N and S will be clearly visible in STEM-EDX and XPS analysis. Hence, it is proved that the N and S are incorporated in an anatase  $\text{TiO}_2$  lattice (NST NFs). The mesoporous FeSiNST NFs have crystal planes (012), (104), (110), (113), (024), (116), (214), and (300), due to the presence of  $\alpha\text{-Fe}_2\text{O}_3$  [JCPDS no. 33-0664]. The FeSiNST NFs also include some anatase  $\text{TiO}_2$  signature along with N and S, but some peaks of  $\text{TiO}_2$  are overlapped by  $\alpha\text{-Fe}_2\text{O}_3$  peaks. The less intense peaks of FeSiNST NFs are due to the presence of the amorphous nature of  $\text{SiO}_2$ . Hence, mesoporous FeSiNST NFs consists of  $\alpha\text{-Fe}_2\text{O}_3$ ,  $\text{SiO}_2$ , and  $\text{TiO}_2$  along with N and S.

**3.2. Morphological Study.** The SEM images (Figure 2) describe the morphologies of the NFs. The variation of

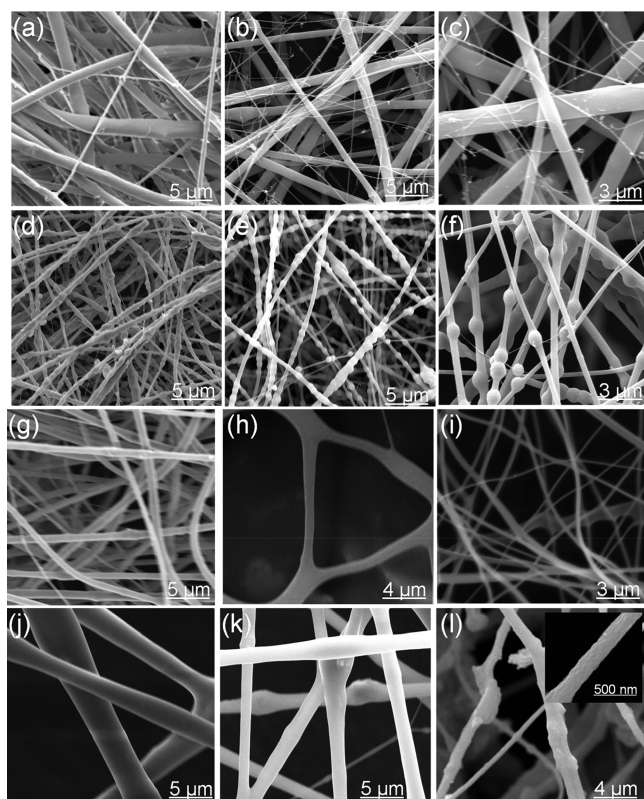


**Figure 2.** Representative SEM images of NFs calcined at different temperatures of 70, 200, and 450 °C:  $\text{TiO}_2$  NFs (a–c),  $\text{SiO}_2$  NFs (d–f), NST NFs (g–i), and FeSiNST NFs (j–l).

temperature, i.e., before calcination (70 °C, 5 h), intermediate temperature (200 °C, 5 h), and calcination (450 °C, 5 h), with respect to morphology has been examined to identify the stability of the NFs. The heat treatment of NFs at 70 and 200 °C is denoted as PVP and CTAB mixed NFs, whereas calcination at 450 °C is referred to as mesoporosity within NFs. The temperature variation of NFs has been done separately. Figure 2, parts a, b, and c, displays the SEM images of  $\text{TiO}_2$  NFs at 70, 200, and 450 °C, respectively. The smooth, bead-free NFs morphology having black color in Figure 2a,b is due to the PVP and CTAB mixed  $\text{TiO}_2$  NFs. After calcination at 450 °C for 5 h (complete elimination of PVP and CTAB), the mesoporous  $\text{TiO}_2$  NFs are obtained (Figure 2c). The mesoporosity of the NFs is not clearly visible which is due to

the narrow  $P_s$ . The  $\text{TiO}_2$  NFs diameters are at different temperatures are calculated and shown in Table S1. The NFs diameter is reduced gradually from  $500 \pm 50$  to  $210 \pm 30$  nm with variation of temperature from 70 to 450 °C. Similarly, smooth and bead-free PVP and CTAB mixed  $\text{SiO}_2$  NFs are fabricated at the temperatures 70 and 200 °C (Figure 2d,e). Mesoporous  $\text{SiO}_2$  NFs having diameter of  $180 \pm 20$  nm are obtained when PVP and CTAB mixed  $\text{SiO}_2$  NFs are calcined at 450 °C, 5 h (Figure 2f). The diameter decrease of PVP and CTAB mixed  $\text{SiO}_2$  NFs to mesoporous  $\text{SiO}_2$  NFs with different temperatures is shown in Table S1. Likewise, smooth and bead-free PVP and CTAB mixed SNT NFs obtained at heat treatment at 70 and 200 °C are shown in Figure 2g,h. But mesoporous NST NFs having diameter of  $150 \pm 20$  are obtained after calcinations of PVP and CTAB mixed SNT NFs at 450 °C, 5 h (Figure 2i). Moreover, PVP and CTAB mixed FeSiNST NFs having smooth and bead-free morphology are obtained at 70 and 200 °C (Figure 2j,k). But mesoporous FeSiNST NFs having diameter of  $200 \pm 20$  are fabricated, when PVP and CTAB mixed FeSiNST NFs are calcined at 450 °C (Figure 2l). The decrease occurred gradually from 70 to 450 °C (Table S1). From SEM images for all NFs materials, the mesoporosity is not clearly seen which is due to the narrow  $P_s$  in the range 2.5–4.7 (Table S1). From the SEM analyses, it is well-understood that mixed PVP and CTAB have a proficient role in the formation of fiber, whereas different heat treatments have an important role in the creation of mesoporosity in the framework of NFs.

To recognize the importance of mixed PVP and CTAB as a template/surfactant for the construction of mesoporosity within NFs, the FeSiNST has been synthesized separately by taking PVP and CTAB as template and surfactant, respectively. The SEM image of the electrospun FeSiNST, synthesized by only PVP as template, is shown in the Supporting Information (Figure S1a,b). A hierarchical NFs morphology is obtained which is called FeSiNST hierarchical NFs (FeSiNST HNFs). The SEM image of the FeSiNST which is synthesized by only CTAB as surfactant is pictured in Figure S1c,d. Figure S1c illustrates the nanoparticles (NPs) nature, whereas Figure S1d represents the mesoporosity. Hence, FeSiNST synthesized by CTAB is called FeSiNST mesoporous NPs (FeSiNST MNPs). From SEM images of FeSiNST HNFs and FeSiNST MNPs, it is observed that template PVP generates hierarchical NFs and CTAB aids to create mesoporous NPs. For more clarification regarding role of PVP and CTAB, the  $\text{N}_2$  adsorption–desorption isotherm of FeSiNST HNFs and FeSiNST MNPs is pictured in Figure S2. Both materials showing type IV mesoporosity. But the  $S_A$  values of FeSiNST HNFs and FeSiNST MNPs are 95 and 190  $\text{m}^2/\text{g}$ , respectively (Table S1). Mesoporosity is directly related to the  $S_A$ , which means highly mesoporous materials have large  $S_A$  values. Hence, FeSiNST MNPs have a higher mesoporosity than FeSiNST HNFs, which leads to enhanced  $S_A$ . Therefore, the decrease of all NFs diameters with the increase of temperature is owing to the gradual elimination/decomposition of PVP, whereas generation of mesoporosity is due to the decomposition of CTAB at high calcination temperature (450 °C in 5 h). Conclusively, from SEM and  $\text{N}_2$  adsorption–desorption method it is well-understood that PVP is responsible for the preparation of NFs morphology, whereas CTAB is responsible for formation of mesoporosity. The combination of PVP and CTAB is the reason for the creation of mesoporosity within NFs.

In order to study the morphology of the NFs material, TEM and STEM analyses have been executed (Figure 3). Figure 3a,b

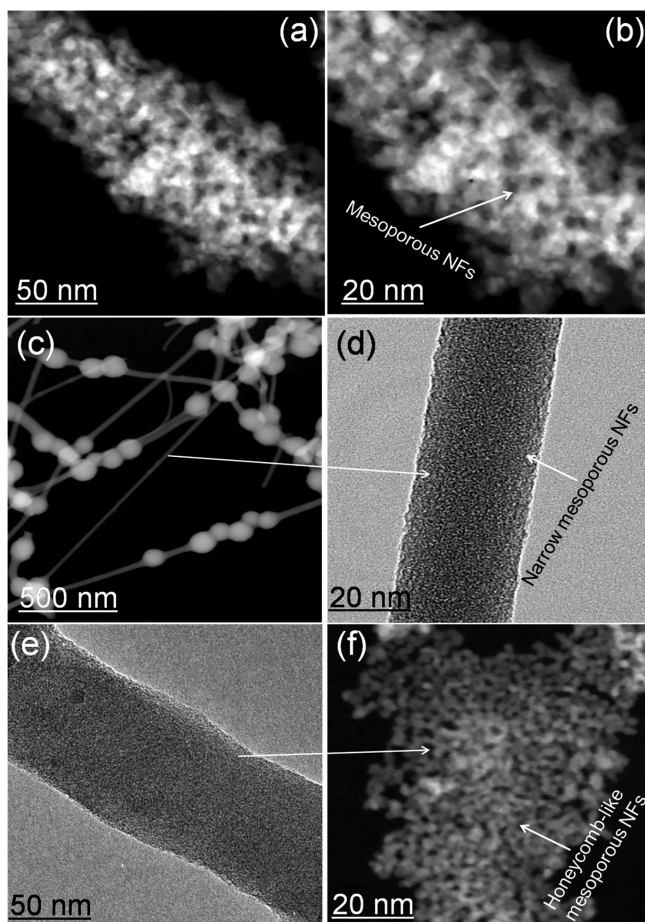


**Figure 3.** Representative TEM images of (a, b) mesoporous TiO<sub>2</sub> NFs, (c, d) mesoporous SiO<sub>2</sub> NFs, and (e, f) mesoporous NST NFs.

depicts STEM micrographs of mesoporous TiO<sub>2</sub> NFs. The morphology of highly porous nature (mesoporous) is observed which is consistent with the N<sub>2</sub> adsorption–desorption study. The diameter of the NFs is  $84 \pm 4$  nm (Table S1). The architecture of the TiO<sub>2</sub> NFs could be “mesoporosity-in-TiO<sub>2</sub> NFs”. Similarly, STEM (Figure 3c) and TEM (Figure 3d) images display the narrow mesoporous nature of NFs with NFs diameter of  $72 \pm 3$  nm and possess “mesoporosity-in-SiO<sub>2</sub> NFs” architecture. Moreover, TEM (Figure 3e) and STEM (Figure 3f) images of the mesoporous NST NFs also retain “mesoporosity-in-SNT NFs” architecture with  $95 \pm 4$  nm NFs diameter. An amazing honeycomb-like mesoporosity is obtained in Figure 3f. Hence, mesoporosity within NFs morphology in all synthesized NFs will increase the surface active sites for photocatalysis performance. HR-TEM images are related to lattice fringes, and SAED patterns of the TiO<sub>2</sub> NFs are pictured in Figure S3a. The lattice space 0.351 nm proves the anatase TiO<sub>2</sub> for the (101) plane in the mesoporous TiO<sub>2</sub> NFs (inset). The SAED image reveals the diffraction patterns for (101), (004), (200), (105), and (211), which are due to the crystalline anatase TiO<sub>2</sub>. Figure S3b defines the amorphous SAED picture of the mesoporous SiO<sub>2</sub> NFs. This is because of the absence of a ring pattern. The SAED pattern (Figure S3c) proves the crystalline nature of the NST NFs and the plane (103) is responsible for N. The lattice spacing of

SNT NFs is 0.345 nm (Figure S3c, inset). The decrease of the lattice spacing from 0.351 nm (TiO<sub>2</sub> NFs) to 0.345 nm (NST NFs) is may be due to the dual incorporation of N and S into the TiO<sub>2</sub> lattice.

The TEM, STEM, and HR-TEM micrographs of mesoporous FeSiNST NFs are presented in Figure 4. A honeycomb-

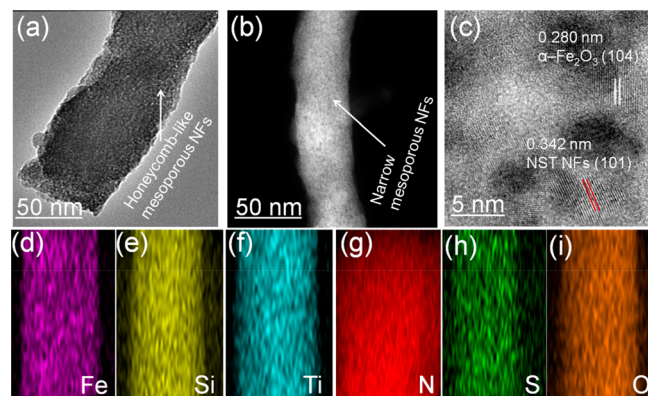


**Figure 4.** Mesoporous FeSiNST NFs: (a) TEM image, (b) STEM image, (c) lattice fringes (HR-TEM), and (d–i) EDX mapping patterns.

like and narrow mesoporosity within NFs have been identified in TEM and STEM images in Figure 4, parts a and b, respectively, which is consistent with N<sub>2</sub> adsorption–desorption study. From TEM and STEM images, the diameter of the NFs is measured as  $84 \pm 3$  nm (Table S1), which is in the nano range. Therefore, the architecture “mesoporosity-in-FeSiNST NFs” is created as in TiO<sub>2</sub> NFs, SiO<sub>2</sub> NFs, and SNT NFs. The lattice space (Figure 4c) of 0.342 nm for NST (101), and 0.280 nm for  $\alpha$ -Fe<sub>2</sub>O<sub>3</sub> (104) are calculated for FeSiNST NFs.<sup>27</sup> The diminution in lattice spacing in NST NFs within FeSiNST than in neat NST NFs is because of the creation of FeSiNST NFs. The lattice borders represent the polycrystalline nature, which is owing to the existence of  $\alpha$ -Fe<sub>2</sub>O<sub>3</sub>, SiO<sub>2</sub>, N, S, and TiO<sub>2</sub>. The unavailability of SiO<sub>2</sub> lattice fringes in FeSiNST NFs (Figure 4c) is due to amorphous nature, which is consistent with XRD measurement (Figure 1c). The polycrystalline nature of FeSiNST NFs is also supportive for harvesting visible light. The dispersal of metal atoms and reactive sites on mesoporous FeSiNST NFs has been confirmed from EDX mapping (Figure 4d–i). It is observed that Fe, Si, Ti, N, S, and O are available in the FeSiNST NFs. STEM-EDX elemental study also supports the presence of individual metal atoms in mesoporous TiO<sub>2</sub> NFs, SiO<sub>2</sub> NFs, NST NFs, and FeSiNST NFs in Figure S4a–d.

**3.3. Optical Analyses.** The UV–vis–NIR diffuse reflectance spectra of all NFs are exposed in Figure 5a. For TiO<sub>2</sub> NFs and SiO<sub>2</sub> NFs samples, the strong reflectance edge which is less than 400 nm corresponds to anatase TiO<sub>2</sub> and amorphous SiO<sub>2</sub>, respectively. The shifting of band edge, i.e., greater than 400 nm in the case of NST NFs and FeSiNST NFs, is because of the long-range visible light absorption. The wide visible light absorption is because of the replacement of N and S by replacing O atom in TiO<sub>2</sub> lattice (NST NFs). The high shifting of band edge in FeSiNST NFs is owing to the combined effect such as replacement of N and S by O atom in TiO<sub>2</sub> lattice and charge transferral phenomena between  $\alpha$ -Fe<sub>2</sub>O<sub>3</sub> and TiO<sub>2</sub>. Apparently,  $\alpha$ -Fe<sub>2</sub>O<sub>3</sub>, N and S dual incorporation, creates a defect level in between the band gap

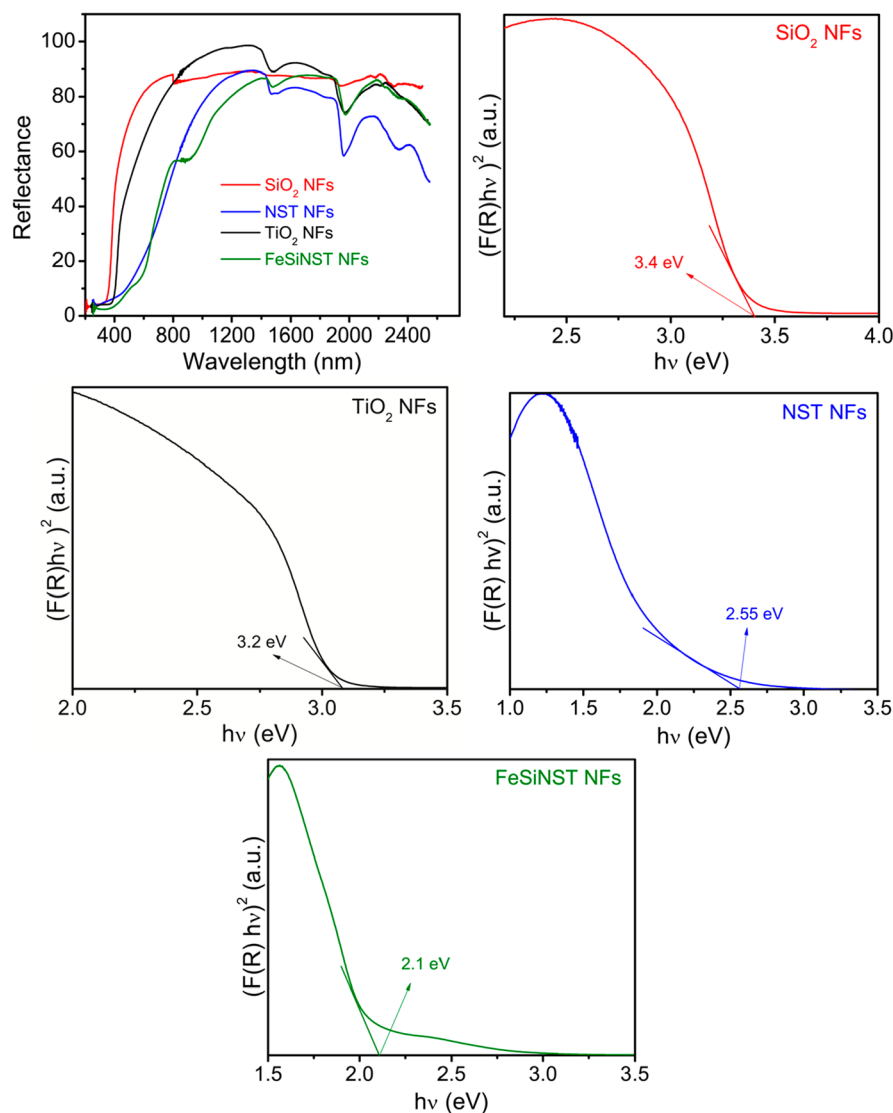


**Figure 5.** UV–vis–NIR DRS and band gap profiles of mesoporous SiO<sub>2</sub> NFs, TiO<sub>2</sub> NFs, NST NFs, and FeSiNST NFs.

of TiO<sub>2</sub> and thus the band edge of the FeSiNST NFs shifting toward the visible region. The formation of  $\alpha$ -Fe<sub>2</sub>O<sub>3</sub> in the mesoporous FeSiNST NFs creates a charge transfer and d–d transition phenomenon which is clearly described in the UV–vis–NIR diffuse reflectance spectra (Figure S5). The FeSiNST NFs show two transition bands: the first range between 496 and 646 nm is ascribed to the 3d electrons (excitation) of Fe<sup>3+</sup> to the conduction band (CB) of TiO<sub>2</sub>. This phenomenon is called the charge transfer transition. Second, the range between 802 and 1041 nm is credited to two transitions: one is the d–d transition of Fe<sup>3+</sup> ( ${}^2T_{2g} \rightarrow {}^2A_{2g}$ ) and the second is the inner charge transfer transition in between Fe<sup>3+</sup> through the CB ( $\text{Fe}^{3+} + \text{Fe}^{3+} \rightarrow \text{Fe}^{4+} + \text{Fe}^{2+}$ ).<sup>22</sup> This infers that involvement of Fe<sup>3+</sup> from  $\alpha$ -Fe<sub>2</sub>O<sub>3</sub> along with N and S in the TiO<sub>2</sub> lattice brings two electronic states, i.e., Fe<sup>4+</sup> and Fe<sup>2+</sup>, in between the band gap of TiO<sub>2</sub>. This phenomenon enhances high light absorption and red shifting in the mesoporous FeSiNST NFs than other NFs photocatalysts. Hence, it is concluded that N and S dual incorporated TiO<sub>2</sub> NFs (NST NFs) favor red shifting due to the substitutional effect, whereas mixing of  $\alpha$ -Fe<sub>2</sub>O<sub>3</sub> as catalytic promoter, and dual N and S in FeSiNST NFs, favors red shifting. The red shifting is due to the charge

transfer transition, d–d transition, and substitutional effect. The red shifting phenomenon enables superior visible light photocatalysis application. The combined Kubelka–Munk [ $K-M/F(R)$ ] and Tauc equation is employed to evaluate the band gap energy of the NFs samples.<sup>28</sup> The detailed explanation is included in the Supporting Information. The band gap energies of all the NFs photocatalysts are given in Figure 5. The band gap of SiO<sub>2</sub> NFs is 3.4 eV (Figure 5), which indicates inactive samples in visible light. The band gap of 3.2 eV is calculated for mesoporous TiO<sub>2</sub> NFs, which indicates the anatase phase and UV-responsive material. The band gap of 2.55 eV is calculated for mesoporous NST NFs, which is smaller than that for TiO<sub>2</sub> NFs. Hence, the band gap lowering is because of the creation of a localized state by intermixing of 2p orbitals of N, S, and Ti. The lowest band gap energy of FeSiNST NFs (2.1 eV) is because of the intermixing of 2p orbitals of Fe, Si, N, S, and Ti, resulting in a localized state. These localized states are created in between the valence band (VB) and the conduction band (CB) which is lowering the band gap. Moreover,  $\alpha$ -Fe<sub>2</sub>O<sub>3</sub> in FeSiNST NFs has a vital role in decreasing the band gap energy which is because of d–d transition and charge transfer phenomena.

To evaluate charge transfer phenomena, recombination of  $e^- - h^+$ , and vacancy in semiconductor NFs, photoluminescence (PL) emission spectra have been pictured. The PL spectra of all NFs materials are generated with an excitation wavelength of  $\lambda_{exc} = 390$  nm, and the result is pictured in Figure 6a,b. In

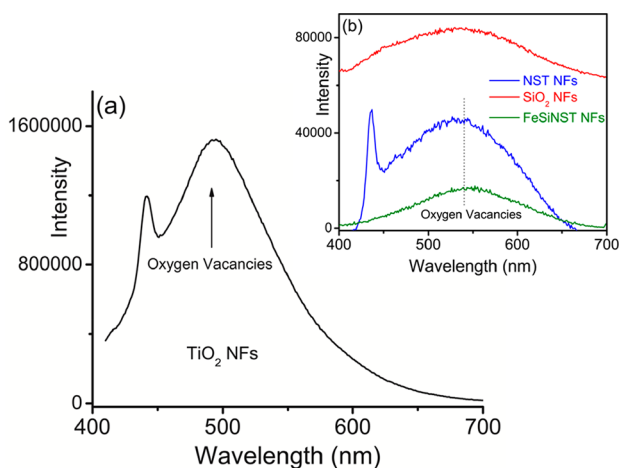


**Figure 6.** (a) PL spectra of mesoporous  $\text{TiO}_2$  NFs and (b) mesoporous  $\text{SiO}_2$  NFs, NST NFs, and FeSiNST NFs.

Figure 6a, two peaks around 440 and 495 nm are observed for  $\text{TiO}_2$  NFs. The emission band situated at 440 nm is because of the surface trapped recombination.<sup>29</sup> The peak at 495 nm (emission) can be consigned to the bulk defects trapped recombination. This peak appears due to the occurrence of impurities in the  $\text{TiO}_2$  NFs.<sup>30</sup> The impurities are due to the  $\text{O}_{vs}$  which are created under the CB of the  $\text{TiO}_2$  NFs.<sup>31</sup> The PL spectrum of mesoporous  $\text{SiO}_2$  NFs (Figure 6b) shows a broad peak around 450–600 nm which is due to the amorphous nature of the  $\text{SiO}_2$ .<sup>32</sup> The PL peaks of the semiconductor NST NFs and FeSiNST NFs are lower than those of the  $\text{TiO}_2$  NFs (Figure 6a,b). It is recognized that the PL emission depicts the recombination of excited  $e^- - h^+$ . Thus, decrease in PL intensity confirms a lower recombination rate of  $e^-$  and  $h^+$ .<sup>33</sup> The least recombination of  $e^- - h^+$  favors the superior photocatalysis performance. The semiconductor FeSiNST NFs has the least  $e^- - h^+$  recombination compared with other synthesized NFs. Hence, FeSiNST NFs will act as a proficient photocatalyst for the photoreduction of Cr(VI), and the photodegradation of 4-NP and phenol. Additionally, the least  $e^- - h^+$  recombination of FeSiNST NFs is because of the formation of  $\text{O}_{vs}$ , d–d transition, and charge transfer transition.<sup>34</sup> The  $\text{O}_{vs}$  of the NST NFs and FeSiNST NFs are pictured in Figure 6b. Mesoporous NST NFs and FeSiNST NFs show  $\text{O}_{vs}$  at 540 nm. The N and S dual incorporation into  $\text{TiO}_2$  (NST NFs) leads to the construction of  $\text{Ti}^{3+}$ . The photoemission electrons are trapped by  $\text{Ti}^{3+}$  from the CB of  $\text{TiO}_2$  through nonradiative transition. Further, the  $\text{O}_{vs}$  help to accept the excited electrons, while the  $h^+$  are trapped by the N and S. Moreover, the excited electrons can also be transferred from the VB to the new defect level which are introduced by N and S that are situated below the CB. This process inhibits the recombination of  $e^- - h^+$  and the resulting swift photoreduction and photodegradation in visible light. Furthermore, a high rate of interfacial charge transfer favors quantum confinement which is because of the enhanced thermodynamic energy of the confined  $e^- - h^+$  pairs.<sup>35</sup> The creation of interfacial charges

in the FeSiNST NFs is due to the existence of  $\text{Fe}^{3+}$  ( $\text{Fe}^{3+} + \text{Fe}^{3+} \rightarrow \text{Fe}^{4+} + \text{Fe}^{2+}$ ). Technically, the compensation of electrons within Fe ions leads to  $e^- - h^+$  recombination. This phenomenon benefits decreasing the  $e^- - h^+$  recombination, resulting in lowering the PL intensity over other NFs. In d–d transition phenomena,  $\text{Fe}^{3+}$  ions can acquire lattice locations by replacing  $\text{Ti}^{4+}$  ions or can be placed in interstitial positions, whereas the  $\text{O}_{vs}$  help to maintain the electrical charge balance. The depletion of peak intensity in the FeSiNST NFs is due to the  $\text{O}_{vs}$  which are involved in charge/electrical balance phenomena. Thus, in FeSiNST NFs, the formation of interfacial charge transfers and d–d transitions has a vital role in decreasing PL intensity and suppressing  $e^- - h^+$  recombination. Conclusively, N and S dual incorporated  $\text{TiO}_2$  generates  $\text{O}_{vs}$ , whereas involvements of  $\alpha\text{-Fe}_2\text{O}_3$  (FeSiNST NFs) generate charge transfer transition and d–d transition. This process really helps to lower  $e^- - h^+$  recombination and enhance photocatalysis activity.

**3.4. Chemical Structure Analyses.** The XPS study of mesoporous FeSiNST NFs is performed in Figure 7. In

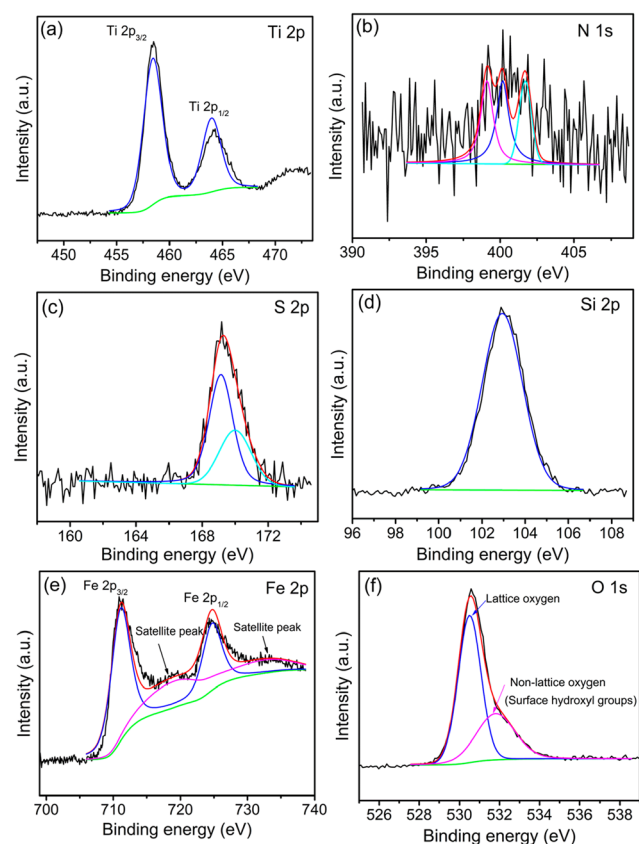


**Figure 7.** Core level spectra of Ti 2p (a), N 1s (b), S 2p (c), Si 2p (d), Fe 2p (e), and O 1s (f) in mesoporous FeSiNST NFs.

FeSiNST NFs, the binding energy (BE) values are situated at 458.4 and 464.1 eV for the peaks  $\text{Ti } 2p_{3/2}$  and  $\text{Ti } 2p_{1/2}$ , respectively (Figure 7a). But the BE values of  $\text{Ti}^{4+}$  in neat  $\text{TiO}_2$  are also calculated, which appear around 459.3 and 464.8 eV (Figure S6) for the peaks  $\text{Ti } 2p_{3/2}$  and  $\text{Ti } 2p_{1/2}$ , respectively.<sup>36</sup> The downshift of  $\text{Ti}^{4+}$  BE in FeSiNST NFs compared with neat  $\text{TiO}_2$  indicates the simultaneous electron transfer from N and S to Ti (forming  $\text{Ti}^{3+}$  environment). Another situation is electron transfer from O atom ( $\alpha\text{-Fe}_2\text{O}_3$  and  $\text{SiO}_2$ ) to Ti. This

is because of the electronegative and electropositive differences between O and Ti, respectively. The aforesaid factors are the vibrant reason for the reduction of  $Ti^{4+}$  to  $Ti^{3+}$  in the FeSiNST NFs which enable visible light shifting. The peak at 399 and 400 eV (Figure 7b) is due to the presence of N in the bonding type of O–Ti–N and Ti–N–O through substitutional and interfacial combinations, respectively. This N incorporation formed the N 2p localized state in between the VB and the CB of  $TiO_2$ , resulting in visible light absorption. This process enables an efficient photocatalysis performance under visible light. The N 1s peak around at 401.6 eV is ascribed to the existence of N in oxidized state, which may form –Ti–N–O–, –Ti–O–N– linkage. This oxidized N forms a close interaction toward O, which is favorable for an interstitial N incorporation.<sup>37</sup> Hence, the bonding framework of –Fe–O–N– and –Si–O–N– may be likely in FeSiNST NFs. The keen observation is that, in the FeSiNST NFs, the substitution of N by O is a vital aspect because of the presence of  $TiO_2$ ,  $\alpha$ - $Fe_2O_3$ , and  $SiO_2$ . In the S 2p spectrum (Figure 7c) two peaks appear at 169.1 and 170 eV, conforming to  $S^{6+}$ .<sup>38</sup> Hence, S atom is incorporated into the FeSiNST mainly as  $S^{6+}$ . It has been observed that replacement of  $Ti^{4+}$  by  $S^{6+}$  is more facile and suitable, when thiourea is used as the sulfur source.<sup>39</sup> It has been examined that the substitution of  $Ti^{4+}$  by  $S^{6+}$  generates  $O_{vs}$  in the  $TiO_2$  lattice.<sup>40</sup> Thus, in the present study, S is incorporated into the FeSiNST NFs in the form of substitution of  $Ti^{4+}$  by  $S^{6+}$ , which creates  $O_{vs}$ . Hence, the generation of  $O_{vs}$  is also proved by XPS analysis. It is noted that the BE of Si 2p in neat  $SiO_2$  is 103.7 eV.<sup>41</sup> But in the present study the BE of Si 2p ( $Si^{4+}$ ) in the FeSiNST NFs is 102.9 eV (Figure 7d). The downshift of BE is owing to the transfer of electrons from N to  $Si^{4+}$  which causes an increase of electron density over  $Si^{4+}$ . It is also well-known that the two characteristic BEs at 712.1 eV (Fe  $2p_{3/2}$ ) and 725.5 eV (Fe  $2p_{1/2}$ ) and a satellite peak at 719.1 eV are because of the  $\alpha$ - $Fe_2O_3$ .<sup>42</sup> In the present investigation, the peaks are at 711.1 and 724.8 eV analogous to the Fe  $2p_{3/2}$  and Fe  $2p_{1/2}$ , respectively, along with the two satellite peaks are at nearly 719 and 724.8 eV, proving the existence of  $\alpha$ - $Fe_2O_3$  in the FeSiNST NFs (Figure 7e). The low BE shifting of Fe 2p in FeSiNST NFs compared with pure Fe 2p is because of the electron transfer from  $Ti^{4+}$  to  $Fe^{3+}$  and the generated –Ti–O–Fe– bonding framework. The electron transfer from  $Ti^{4+}$  to  $Fe^{3+}$  is due to the electronegativity differential between  $Fe^{3+}$  (1.83) and  $Ti^{4+}$  (1.54). Hence, the electron density of  $Ti^{4+}$  ion is lower than that of  $Fe^{3+}$ . This phenomenon enables the rise of the BE of  $Ti^{4+}$  and the fall of the BE of  $Fe^{3+}$ . The BE of O 1s (Figure 7f) in FeSiNST NFs is located at 530.5 eV, owing to the lattice oxygen, suggesting the existence of Ti–O bonding in  $TiO_2$ .<sup>43</sup> The peak at ca. 531.8 eV (nonlattice oxygen) is because of the surface hydroxyl available in the FeSiNST NFs. Additionally, the peak at 531.8 eV is also ascribed to the presence of –S–O–S– linkage.<sup>38</sup> It has been also observed that the rise in the area of nonlattice oxygen specifies the creation of  $O_{vs}$ .<sup>44</sup> In Figure 7f, the peak area of the nonlattice oxygen is nearly half that of the lattice oxygen, which also proves the generation of the  $O_{vs}$  in  $TiO_2$  lattice (FeSiNST NFs).

**3.5. Electrochemical Performance.** The photoelectrochemical study of mesoporous FeSiNST NFs along with NST NFs has been studied (Figure 8). In order to measure the photocurrent, charge density, and rate of charge transfer at the electrode/electrolyte interface within NFs, the photocurrent measurement, MS (Mott–Schottky) diagram, and EIS

(electrochemical impedance spectroscopy) are studied, respectively. The photocurrent of mesoporous NST NFs and FeSiNST NFs is measured in 0.1 M  $Na_2SO_4$  (0.1 M) at 10 mV  $s^{-1}$  scan rate in  $\lambda \geq 400$  nm. The photocurrent densities, i.e., 1.8 and 3.2 mA/cm<sup>2</sup>, are calculated for mesoporous NST NFs and FeSiNST NFs, respectively (Figure 8a). The photocurrents in both NFs with positive values represent the anodic direction with the applied potential, resulting in n-type semiconductors. The mesoporosity within NFs has a key role in a proficient harvest of photocurrent in both NFs. The harvesting of higher photocurrent in FeSiNST NFs than in NST NFs is owing to the efficient charge transport within NFs.<sup>45</sup> The superior charge transport in FeSiNST NFs is because of  $\alpha$ - $Fe_2O_3$ . This efficient charge transport is because of the d–d transition and charge transfer transition, which leads to enhancement of the electron mobility or electron density. The high electron mobility over FeSiNST NFs increases the photocatalysis performance.

The MS method has been used to check the band arrangement and recombination properties. This process is calculated in three-electrode systems using the counter electrode (Pt) and reference electrode (Ag/AgCl), and both are dipped in  $Na_2SO_4$  (0.1 M) in 1000 Hz at pH 6.5 in the dark. Figure 8b–d represents the MS diagram of  $\alpha$ - $Fe_2O_3$  NFs, NST NFs, and FeSiNST NFs. The SEM image and the EDX elemental analysis of  $\alpha$ - $Fe_2O_3$  NFs has been inserted in Figure S7. The positive slope for all samples shows n-type semiconductor behavior. The mesoporous FeSiNST NFs having a single slope specifies that  $\alpha$ - $Fe_2O_3$  is crucially promoted in the photocatalysis activity with N and S dual incorporated  $TiO_2$ . Moreover, from the intercept of the MS diagram (Figure 8b–d), the  $E_{fb}$  (flat band potentials) for  $\alpha$ - $Fe_2O_3$  NFs, NST NFs, and FeSiNST NFs are calculated as –0.61, –0.78, and –1.0 V, respectively. A higher magnitude of negative value for the  $E_{fb}$  in semiconductor (n-type) specifies enhanced transport and separation of charge carriers at the interface of electrolyte–electrode, resulting in enriched photoelectrochemical performance.<sup>46</sup> The FeSiNST NFs have a more negative  $E_{fb}$  than NST NFs and  $\alpha$ - $Fe_2O_3$  NFs. Thus, separation and transport of charge carriers is better facilitated in FeSiNST NFs, which thereby exhibit a better photoelectrochemical response. This process makes the photocatalysis applications excel. It is understood that mixing of metal ions with increased valence states such as  $Ti^{4+}$  and  $Si^{4+}$  results in enhanced electron density on  $\alpha$ - $Fe_2O_3$ , by acting as donor.<sup>47</sup> The low impedance for the FeSiNST NFs is because of the high charge density is directly related to the conductance, which is calculated by the formula  $\sigma = ne_0\mu$ . The better conductivity (electrical) may spread the lifespan of charge carriers, which helps to decrease the  $e^-$ – $h^+$  recombination.<sup>48</sup> Thus, the enhanced charge density and lower  $e^-$ – $h^+$  recombination in the surface by the mixing of Ti and Si surface is supposed to be the key aspect for the remarkable photocurrent enhancement of the  $\alpha$ - $Fe_2O_3$  in the FeSiNST NFs. The CB potential for n-type semiconductors is nearly equal to  $E_{fb}$ . Hence, the locations of the CB for  $\alpha$ - $Fe_2O_3$  NFs and NST NFs are –0.61 and –0.78 V, respectively. Thus, band structure has significant role in the high photocatalysis performance, which is reflected in the photocatalysis section.

The semicircles at higher frequency and the nearly straight line at the lower frequency level (Nyquist plots) are observed in the EIS of mesoporous NST NFs and FeSiNST NFs (Figure 8e). The low frequencies (semicircle) represent the charge

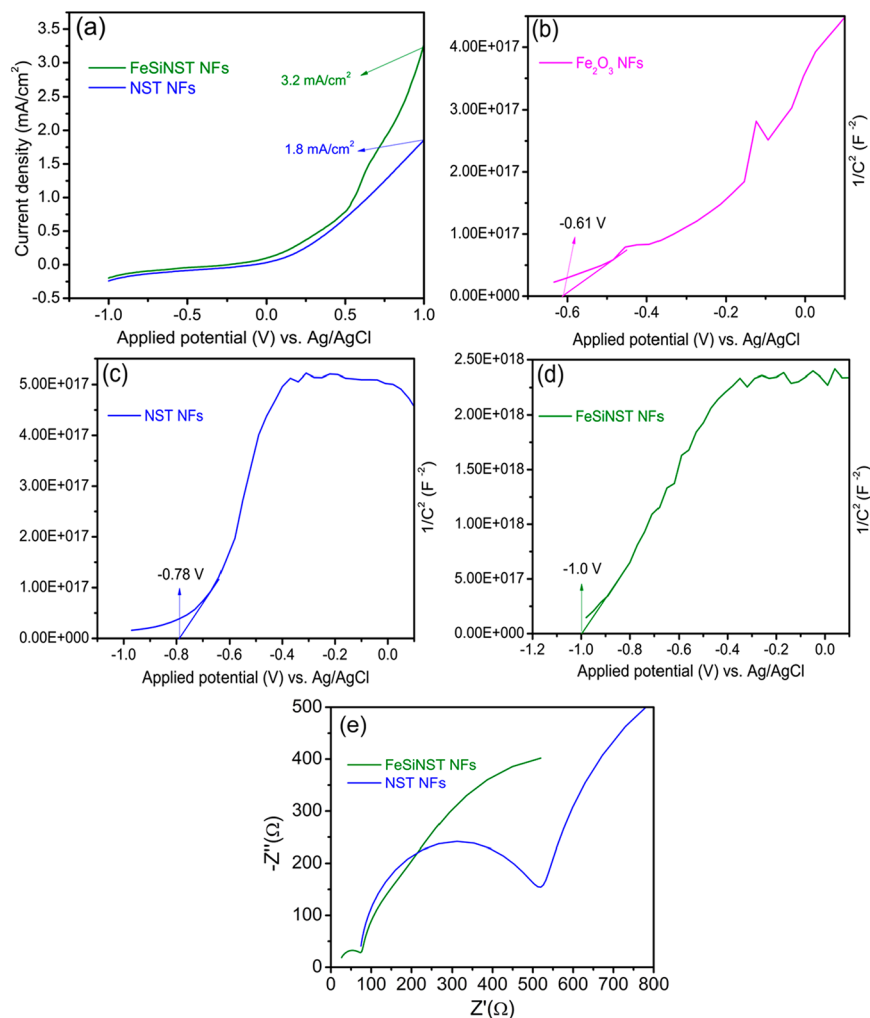


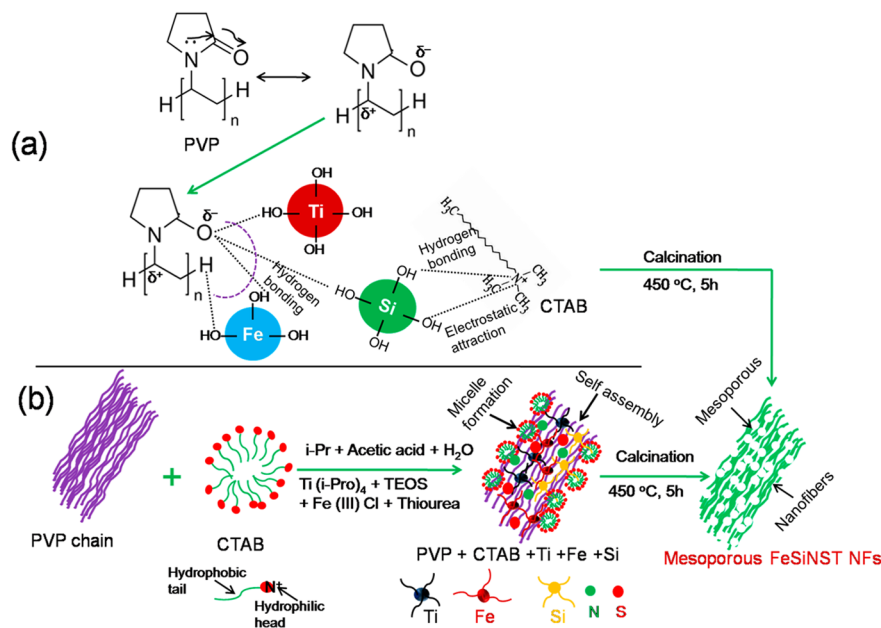
**Figure 8.** Potential–current density curves of mesoporous NST NFs and FeSiNST NFs (a) under light condition. MS diagrams of  $\text{Fe}_2\text{O}_3$  NFs, mesoporous NST NFs, and FeSiNST NFs (b–d) in the dark. Nyquist plot for NST NFs and FeSiNST NFs (e).

transfer within the electrode/electrolyte interface, whereas the charge transfer resistance ( $R_{ct}$ ) is calculated from the semicircle diameter.<sup>49</sup> In the present investigation, the  $R_{ct}$  value for mesoporous NST NFs ( $\sim 516 \Omega$ ) is greater than that for the FeSiNST NFs ( $\sim 74 \Omega$ ). It is noted that the bigger semicircle diameter provides the high resistance at the interface, which shows less conductance. The lower  $R_{ct}$  of the FeSiNST NFs is due to the modification of the  $\alpha\text{-Fe}_2\text{O}_3$  which facilitates the facile charge momentum within the interface, thus increasing generation of photocurrent. The lesser  $R_{ct}$  value indicates the greater charge transfer performance in mesoporous FeSiNST NFs. Charge transfer phenomena may progress capably from  $\text{TiO}_2$  ( $\text{Ti}^{4+}$ )/ $\text{SiO}_2$  ( $\text{Si}^{4+}$ ) to  $\alpha\text{-Fe}_2\text{O}_3$  ( $\text{Fe}^{3+}$ ). The charge transfer toward  $\alpha\text{-Fe}_2\text{O}_3$  ( $\text{Fe}^{3+}$ ) is because of internal charge transfer transition and d–d transition (Figure S5) which creates vacant sites within  $\alpha\text{-Fe}_2\text{O}_3$ . Thus,  $\alpha\text{-Fe}_2\text{O}_3$  becomes the charge trap center in FeSiNST NFs. Henceforth, the FeSiNST NFs have a more effective  $e^-$ – $h^+$  separation than SNT NFs. Thus, FeSiNST NFs will have superior photocatalysis activity which is due to the low  $R_{ct}$  value. Furthermore, in the lower frequency region, a straight line is observed which is due to the  $W_s$  (Warburg impedance). This  $W_s$  is responsible for the diffusion or transfer of ions within an electrolyte.<sup>50</sup> The FeSiNST NFs have a lower Warburg region

than NST NFs (Figure 8e). The smaller Warburg region of the mesoporous FeSiNST NFs is due to the effective ion movement in the NFs via mesopores and supports superior photocatalysis performance. Hence, enriched current density, charge transfer, and ion momentum in the FeSiNST NFs are the key factors for the improved photocatalysis performance which is because of the mixing of  $\alpha\text{-Fe}_2\text{O}_3$  as electron trap center and mesoporosity within NFs.

**3.6. Growth Mechanism.** The growth mechanism of mesoporous FeSiNST NFs is described in the origin of the synthesis procedure (Scheme 2). The mesoporous FeSiNST NFs are synthesized on the basis of the electrospinning via sol–gel method. Scheme 2a depicts the chemical interaction, whereas Scheme 2b describes the schematic approach regarding formation of the mesoporous FeSiNST NFs. The precursors of Ti, Fe, and Si are diluted in the mixed solvents isopropanol and  $\text{H}_2\text{O}$  including PVP and CTAB in acetic acid, and then the hydrolysis process is progressed and forms  $\text{Ti}(\text{OH})_4$ ,  $\text{Si}(\text{OH})_4$ , and  $\text{Fe}(\text{OH})_3$  in the reaction media. These hydroxyl groups make hydrogen bonding with oxygen available in PVP, and also form a hydrogen bond with  $\text{N}^+$  from CTAB. Another possibility is that oxygen atom from metal hydroxide also creates a Coulombic interaction with  $\text{N}^+$ , present in CTAB. The thiourea was also hydrolyzed and the N and S

Scheme 2. Chemical Interaction (a) and Schematic Pathways (b) of Growth Mechanism of Mesoporous FeSiNST NFs



atoms anchor to the metal hydroxides through oxygen and hydrogen. The nucleation of metal particles and formation of sol are created in this process. The PVP and CTAB formed a polymeric chain and micelles with metal hydroxide sol and finally formed a gel for electrospinning, respectively. The mesoporous FeSiNST NFs are formed after drying (70 °C, 3 h) and calcinations (450 °C, 5 h) of PVP and CTAB mixed FeSiNST NFs.

PVP, CTAB, and acetic acid have vital roles for the fabrication of the mesoporous FeSiNST NFs (Scheme 2b). PVP (template) has a long polymeric chain which is responsible for the fabrication of NFs framework during the electrospinning process. Additionally, long chain PVP creates hydrogen bonding with –OH groups of metals such as Ti, Fe, and Si. CTAB is an amphiphilic molecule, which contains a hydrophilic head and a hydrophobic tail. It will form the micelles and subsequent nucleation for the growth of metal (Ti, Fe, and Si) hydroxides. Moreover, after addition of CTAB, the ion pairs are formed due to electrostatic interaction of the active species ( $N^+ \cdots O^{2-}$ ), which speed up the reaction of the growth units. During the evaporation of solvent, the self-assembly of CTAB micelles with metal hydroxides occurred, which led to a complete polymerization of the inorganic network. In the crystallization process, the CTAB serves as a pore growth controller and surfactant. During the calcinations, the CTAB decomposes and organic species are removed, leading to formation of the mesoporous FeSiNST NFs. It is stated that the species which are causing foam during hydrolysis help to produce mesoporosity.<sup>51</sup> The foams are generated after mixing of CTAB in water which leads to formation of a micelle, and resulting mesoporosity within FeSiNST NFs after calcination. The acetic acid in the reaction stabilized the sol. This is because acetic acid has tendency to slow down the condensation and reduce the gelation rate of sol.<sup>52</sup> The optimum amount of the acetic acid in the reaction solution aids to form perfect NFs. Hence, PVP, CTAB, and acetic acid have vital involvement for the synthesis of mesoporous FeSiNST NFs.

### 3.7. Photocatalysis Activity of Mesoporous Nanofibers

Photoreduction of Cr(VI) proceeded under visible light. It is examined that mesoporous FeSiNST NFs have superior Cr(VI) photoreduction performance. The experiment was continued for 80 min in visible light,  $K_2Cr_2O_7$  (40 mg·L<sup>-1</sup>) solution, and catalyst dose (1 mg·mL<sup>-1</sup>). In order to check the effect of pH, the photoreduction of Cr(VI) progressed on different pHs (Figure S8). The photoreduction of Cr(VI) by FeSiNST NFs falls at higher pH. This is because the photocatalyst surface (low pH) gets protonated, resulting in formation of  $HCrO_4^-$  species and enhancing the photoreduction process. The photocatalyst surface becomes negative at high pH, which repels the negative species  $Cr_2O_7^{2-}$ , resulting in low photoreduction activity. The results shows that the highest photoreduction Cr(VI) is at pH 4. Hence, pH 4 is the optimum pH condition for the photoreduction of Cr(VI) by different NFs photocatalysts (Figure 9a). After reaction, the UV–visible absorbance intensity of Cr(VI) diminishes slowly from SiO<sub>2</sub> NFs to FeSiNST NFs. The least absorbance (Figure 9a) in the case of mesoporous FeSiNST NFs specifies proficient photoreduction of Cr(VI).

The photodegradation of 4-NP and phenol progressed under visible light. The reaction is performed in 100 min, 30 mg·L<sup>-1</sup> (4-NP and phenol), and catalyst dose (1 mg·mL<sup>-1</sup>). The effect of pH on the photodegradation of phenol is described in Figure S9. The reactions progressed at different pH by mesoporous FeSiNST NFs. The photodegradation of phenol was maximum at pH 6 (100%), and with a gradual rise of pH from 6 to 10, the percent of photodegradation decreases. This may be described by the acid strength ( $pK_a$ ) of phenol, i.e., 9.8. Generally phenol dissociation starts at pH >  $pK_a$ , so at pH above 9.8, the photodegradation decreases because of phenol ionization, resulting in less photodegradation. The highest photodegradation is observed at pH 6, which is due to the presence of undissociated phenol. Not only phenol but also the photodegradation percent of 4-NP is seen at pH 6. The reason is similar to that for phenol photodegradation.

The photodegradation of 4-NP and phenol by different NFs photocatalysts is presented in Figure 9, parts b and c,

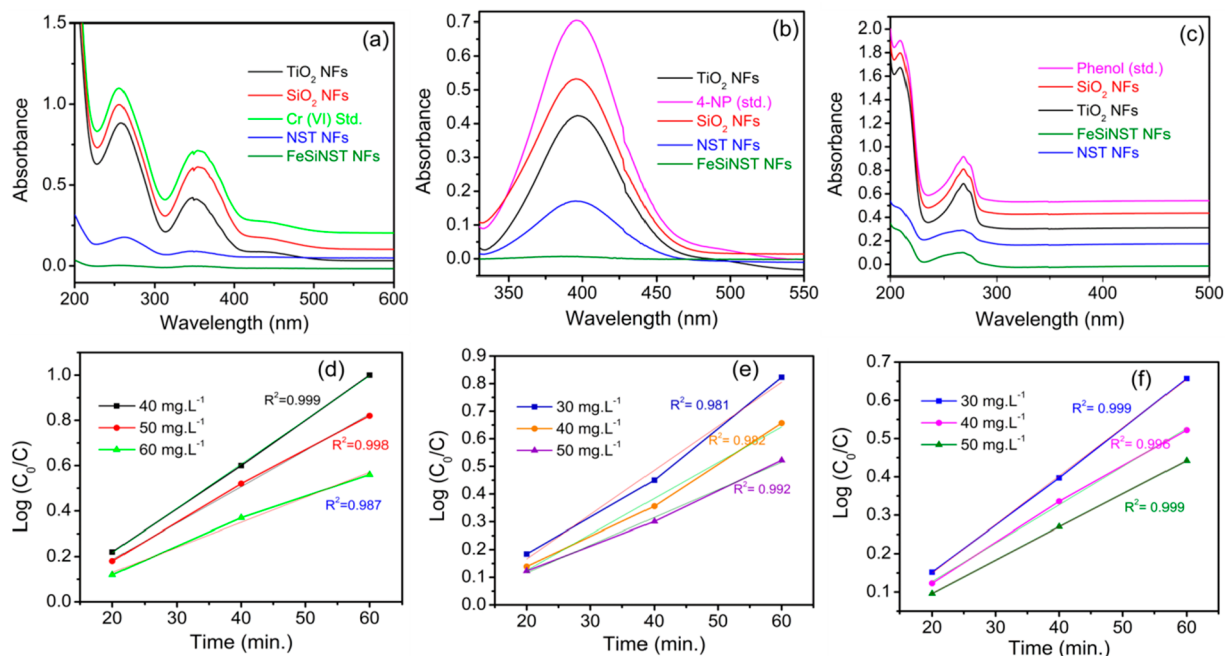


**Figure 9.** UV–vis spectra of solutions recorded after photoreduction Cr(VI) (a), and photodegradation of 4-NP (b) and phenol (c) by different photocatalysts (10 mg in 10 mL solution) under visible light. The photoreduction process is continued at pH 4 in 80 min, whereas the photodegradation process is at pH 6 in 100 min. The kinetic study is also performed by taking different concentrations (40, 50, and 60 mg·L<sup>-1</sup>) for Cr(VI) (d). Concentration varies (30, 40, and 50 mg·L<sup>-1</sup>) for 4-NP (e) and phenol (f), with different time intervals (20, 40, and 60 min) on mesoporous FeSiNST NFs.

respectively. The experiment is performed in 100 min at pH 6 under visible light. The UV–visible absorbance intensity of 4-NP drops from SiO<sub>2</sub> NFs to FeSiNST NFs with respect to 4-NP (standard). The lowest absorbance in the case of FeSiNST NFs indicates efficient photodegradation of 4-NP (Figure 9b). The photodegradation of phenol by different NFs photocatalysts also followed the same trend as 4-NP, i.e., SiO<sub>2</sub> NFs < TiO<sub>2</sub> NFs < NST NFs < FeSiNST NFs. The percent of Cr(VI) photoreduction, and 4-NP and phenol photodegradation, varies with different photocatalysts as displayed in Table S2. The high percent of Cr(VI) photoreduction and 4-NP photodegradation as compared to phenol is detected. This is because of the light yellow color of both Cr(VI) and 4-NP which enables them to absorb visible light proficiently as related to phenol. The increase in photocatalysis (photoreduction and photodegradation) reaction of Cr(VI), and 4-NP and phenol, by mesoporous FeSiNST NFs is because of the mesoporosity within NFs, high light absorption property, charge transfer transition, d–d transition, O<sub>vs</sub>, and e<sup>-</sup>–h<sup>+</sup> separation. The high light absorption property is due to the optimum amount of Ti, N, and S, whereas the optimum amount of Fe enhances the charge transfer transition and d–d transition in FeSiNST NFs. The suitable amount of Si aids in increasing the surface properties for an efficient photoreduction and photodegradation performance.

The mesoporosity within NFs increases the S<sub>A</sub>, and the high S<sub>A</sub> provides fruitful reactive sites for the photocatalysis performance. The mesoporous FeSiNST NFs has a wider S<sub>A</sub>, i.e., 300 m<sup>2</sup>/g, than other synthesized NFs; hence the interaction of reactant species with photocatalyst surface will be more, resulting in high photocatalysis performance. The mesoporous SiO<sub>2</sub> NFs have lower photocatalysis activity despite a high S<sub>A</sub> (500 m<sup>2</sup>/g). This is because of the absence of N and S as visible light absorber and α-Fe<sub>2</sub>O<sub>3</sub> as catalysis

promoter. The enhanced light absorption/red shifting is due to the availability of N and S as visible light absorber in photocatalyst NST NFs and FeSiNST NFs (UV–vis–NIR DRS spectra). But mesoporous FeSiNST NFs have a higher photocatalysis performance than mesoporous NST NFs. Hence, it is understood that α-Fe<sub>2</sub>O<sub>3</sub> has a tremendous role which makes FeSiNST NFs a superior photocatalysis. The d–d transition and charge transfer transition are created owing to the presence of Fe<sup>3+</sup> (α-Fe<sub>2</sub>O<sub>3</sub>) in FeSiNST NFs (UV–vis–NIR DRS spectra). According to crystal field theory, it is known that Fe<sub>2</sub>O<sub>3</sub> has vacant d orbitals. Hence, Fe<sup>3+</sup> in composite FeSiNST NFs can capture electrons through d–d transition, resulting in lowering e<sup>-</sup>–h<sup>+</sup> and enhancing photocatalysis activity. But the charge transfer transition induces Fe<sup>4+</sup> and Fe<sup>2+</sup> electronic states within N and S in the TiO<sub>2</sub> lattice, resulting in an impurity state and decreasing the band gap. This phenomenon enhances the light absorption in visible light. Furthermore, the formation of interfacial charge in the composite FeSiNST NFs is due to the presence of Fe<sup>3+</sup>, which enhances the light absorption property and suppresses the charge recombination. The d–d transition and charge transfer transition phenomenon also enhances the light absorption property and red shift, resulting in high photocatalysis performance in FeSiNST NFs. Although NST NFs have more light absorption property and red shift, the absence of charge transfer phenomena shows less photocatalysis activity than FeSiNST NFs (Figure 9). O<sub>vs</sub> have great ability to capture electrons, which leads to separating e<sup>-</sup>–h, resulting in effective photocatalysis activity.<sup>53</sup> The creation of O<sub>vs</sub> is because of the presence of N and S and α-Fe<sub>2</sub>O<sub>3</sub>. Hence, the availability of O<sub>vs</sub> in FeSiNST NFs (PL and XPS study) supports the efficient photoreduction Cr(VI), and the photodegradation of 4-NP and phenol. The high photocurrent density enables generation of high electrons and holes which support tremendous

photocatalysis performance in FeSiNST NFs compared with NST NFs (electrochemical study, Figure 8). The increase of  $E_{fb}$  in FeSiNST NFs has a greater ability for suppressing  $e^- - h^+$  recombination than NST NFs, resulting in high photocatalysis performance. The small values of  $R_{ct}$  and  $W_s$  (EIS study) enhance charge transfer, charge separation, and ion momentum in the case of FeSiNST NFs, resulting in superior photoreduction of Cr(VI), and photodegradation of 4-NP and phenol compared with other synthesized NFs.

The kinetics of Cr(VI) photoreduction, and 4-NP and phenol photodegradation, by mesoporous FeSiNST NFs is revealed in Figure 9d–f. The outcomes are fitted in  $\log C_0/C$  vs  $t$ . Various concentrations (40, 50, and 60  $\text{mg}\cdot\text{L}^{-1}$ ) of Cr(VI) and the concentrations (30, 40, and 50  $\text{mg}\cdot\text{L}^{-1}$ ) for 4-NP and phenol with time variation (20, 40, and 60 min) for all are studied in the kinetic process. The rate of photocatalysis performance is more at lower concentrations of Cr(VI), 4-NP, and phenol and goes down with a rise of concentration. The concentrations of Cr(VI), 4-NP, and phenol with respect to time achieved a linear relationship. First order kinetics is observed for Cr(VI) photoreduction and for 4-NP and phenol photodegradation. The calculated data are fitted well for first order kinetics, and the equations are as follows.

$$\log C_0/C = Kt/2.303 \quad (1)$$

$$K = (2.303 \log C_0/C)/t \quad (2)$$

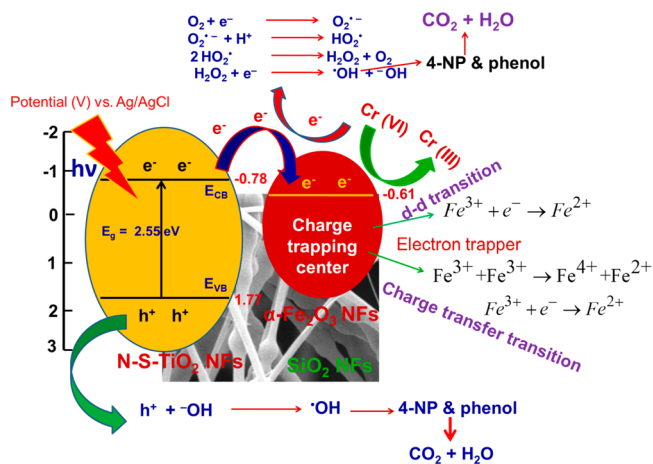
where the first order rate constant is referred to as  $K$ , the Cr(VI) concentration (initial) is attributed as  $C_0$ , and  $C$  stands for the concentration with passage of time ( $t$ ).

The active species involved in the photoreduction of Cr(VI) on FeSiNST NFs is examined by the trapping test, which is illustrated in Figure S10a. It is noted that  $h^+$ ,  $\cdot\text{OH}$ ,  $\text{O}_2^{\cdot-}$ , and  $e^-$  are the reactive species which are involved in photoreduction. The Cr(VI) photoreduction is decreased less (IPA as scavenger) than the reaction executed without scavenger, which proves negligible participation of  $\cdot\text{OH}$  radicals in photoreduction. The photoreduction of Cr(VI) decreased appreciably by using BQ. Therefore,  $\text{O}_2^{\cdot-}$  has some role in the photoreduction process. But the Cr(VI) photoreduction is extremely diminished when DMSO is used as scavenger. That means  $e^-$  has a great role in the photoreduction of Cr(VI) to Cr(III). Categorically,  $e^-$  plays a vital role in the photoreduction of Cr(VI) under visible light. Hence, more association of  $e^-$  in the reaction proves the high separation of  $e^- - h^+$ . The trapping test for the photodegradation of 4-NP is pictured in Figure S10b. The result shows that the photodegradation percentage is highly decreased when IPA is used as  $\cdot\text{OH}$  scavenger as compared to other scavengers such as KI, DMSO, and BQ. Hence,  $\cdot\text{OH}$  has great role in the 4-NP photodegradation. The photodegradation of phenol will also follow the same trend as that of 4-NP. Conclusively,  $e^-$  is the active agent for the photoreduction of the Cr(VI), whereas  $\cdot\text{OH}$  is the active agent for 4-NP and phenol photodegradation.

**3.7.1. Mechanism of Photocatalysis Activity.** Appropriate CB and VB of the semiconductors are essential to study the mechanism of the Cr(VI) photoreduction, and 4-NP and phenol photodegradation. From the MS diagram (Figure 8b), the  $E_{fb}$  for  $\alpha\text{-Fe}_2\text{O}_3$  NFs is  $-0.61$  V which is nearly equal to the conduction band potential ( $E_{CB}$ ) of the  $\alpha\text{-Fe}_2\text{O}_3$  NFs.<sup>50</sup> Hence, the  $E_{CB}$  of  $\alpha\text{-Fe}_2\text{O}_3$  NFs is  $-0.61$  eV, whereas the  $E_{fb}$  for NST NFs is  $-0.78$  V (Figure 8c). Hence the  $E_{CB}$  of NST NFs is

$-0.78$  eV. The calculated band gap, i.e., 2.55 eV, is for NST NFs (Figure 5). Hence, the  $E_{VB}$  (valence band potential) will be 1.77 eV. Scheme 3 depicts the band edge plot of NST NFs.

### Scheme 3. Possible Reaction Mechanism, Charge Separation, and $e^- - h^+$ Transfer in Mesoporous FeSiNST NFs



On the irradiation of visible light, the  $e^- - h^+$  are formed, which are employed in photoreduction and photodegradation processes. In the photocatalysis process, the recombination of  $e^- - h^+$  hinders the reaction efficiency. To avoid this type of problem, a charge trapper center  $\alpha\text{-Fe}_2\text{O}_3$  which is present in mesoporous FeSiNST NFs enables suppression of the  $e^- - h^+$  recombination. The charge trapper phenomenon occurred in both types of transition, i.e., d–d transition and charge transfer transition. In the d–d transition and charge transfer transition phenomena, the photogenerated electrons are trapped by  $\text{Fe}^{3+}$  center (Scheme 3). According to the crystal field theory, the Fe d-orbitals are vacant during the oxidation/reduction reaction process. Therefore, this process is called the electron trapper process and the  $\text{Fe}^{3+}$  in  $\alpha\text{-Fe}_2\text{O}_3$  NFs (FeSiNST NFs) is called the electron trapper center. Hence, both d–d transition and charge transfer transition phenomena are due to the presence of  $\alpha\text{-Fe}_2\text{O}_3$  in the FeSiNST NFs which aids in diminishing the  $e^- - h^+$  recombination and enhancing the photoreduction of Cr(VI) and photodegradation of 4-NP and phenol. Hence mesoporous FeSiNST NFs display the highest photocatalysis performance in visible light (Figure 9). From the active species trapping test (Figure S10a), it is examined that the  $e^-$  is the most active agent for the photoreduction of Cr(VI). The  $\cdot\text{OH}$  is the active agent for the photodegradation of 4-NP and phenol (Figure S10b). Conclusively, efficient separation of  $e^- - h^+$  has a vital role in the photocatalysis performance.

**3.7.2. Recyclability, Stability, and Evidence of Cr(VI) Photoreduction and 4-NP Photodegradation.** The recyclability, stability, and evidence regarding Cr(VI) photoreduction by FeSiNST NFs are shown in Figure 10, parts a, b, and c, respectively. The recyclability experiment is executed in the optimum condition of the photoreduction of Cr(VI). After each run is finished, the mesoporous FeSiNST NFs material is calcined at 450 °C in 5 h in order to remove impurity and make reborn the mesoporosity. The result is nearly similar up to the fourth consecutive run, indicating the reusability of the mesoporous FeSiNST NFs (Figure 10a). The stability test of mesoporous FeSiNST NFs was examined by the SEM image after Cr(VI) photoreduction (Figure 10b). The NFs

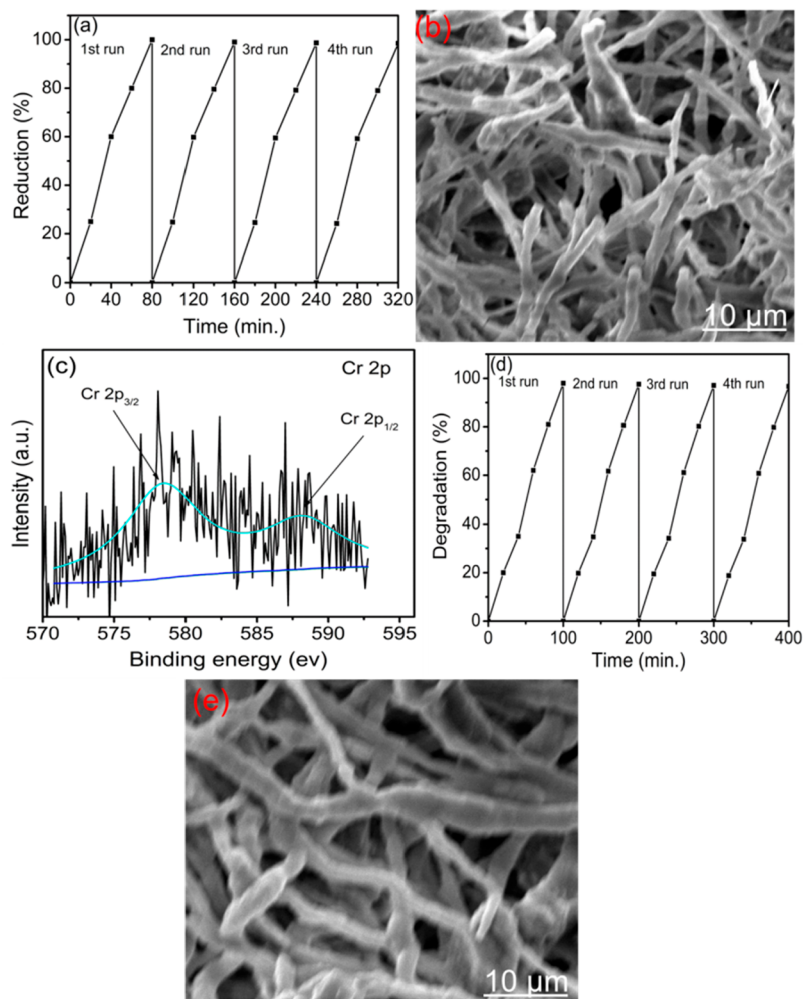


**Figure 10.** (a) Recycling study, (b) stability, and (c) evidence for photoreduction of Cr(VI) in optimum condition. (d) Recycling study and (e) stability of 4-NP photodegradation by mesoporous FeSiNST NFs in optimum condition.

morphology is observed in FeSiNST NFs after the photoreduction of Cr(VI), proving a stable photocatalyst during photoreduction. The Cr 2p spectrum after Cr(VI) photoreduction on FeSiNST NFs is presented in Figure 10c. The BEs at 579.4 and 586.6 eV are referred to the Cr 2p<sub>3/2</sub> and Cr 2p<sub>1/2</sub>, respectively, which are recommended to the Cr 2p in Cr(VI).<sup>54</sup> In Figure 10c, the BEs at 578.2 (Cr 2p<sub>3/2</sub>) and 588.2 eV (Cr 2p<sub>1/2</sub>) match the Cr 2p in Cr(III).<sup>55</sup> This is because of the existence of Cr(III) after the photoreduction of Cr(VI) by FeSiNST NFs. This result gives the evidence for complete photoreduction of Cr(VI) to Cr(III) during the photoreduction process by FeSiNST NFs. Figure 10d describes the recyclability test of 4-NP photodegradation by FeSiNST NFs. The recyclability test is performed in the optimum condition of the 4-NP photodegradation, and after each run the FeSiNST NFs was calcined at 450 °C in 5 h. The result shows that the photodegradation of 4-NP is nearly similar up to the fourth run, indicating the versatility and reusability of the FeSiNST NFs. The stability test of FeSiNST NFs is examined by the SEM image after 4-NP photodegradation (Figure 10e). The NFs morphology is observed in FeSiNST NFs after the photodegradation of 4-NP, indicating that the photocatalyst is stable during reaction.

#### 4. CONCLUSION

PVP and CTAB template/surfactant mixed method is employed for the synthesis of mesoporosity within NFs in all synthesized NFs photocatalysts by the electrospinning via sol-gel process. Formation of enriched mesoporosity within NFs is the important achievement in terms of morphology control. Mesoporosity within NFs provides superior  $S_A$ , mechanical support, and smooth  $e^-$  transport, which is the vital approach of the present study. Mesoporosity within NFs enhances the active sites for a proficient photocatalysis performance. The charge transfer phenomenon includes d-d transition and charge transfer transition enhancing  $e^-$  and  $h^+$  separation effectively. This is the significant reason for an efficient photocatalysis performance. The red shifting and  $O_{vs}$  within photocatalysts increase the long-range light absorption properties and suppress the  $e^-$ - $h^+$  recombination, respectively, also having a marvelous role in photocatalysis. It is established that, among all photocatalysts, mesoporous FeSiNST NFs have the highest photocatalytic activity. The recyclability and stability study in Cr(VI) photoreduction and 4-NP photodegradation support the stability and reusable nature of the FeSiNST NFs photocatalyst. The Cr(VI) photoreduction to Cr(III) by FeSiNST NFs is proved by XPS analysis. The increased photocatalysis activity by mesoporous FeSiNST NFs is

attributed to the  $e^-$  capture by  $Fe^{3+}$  center in visible light, resulting in increases of  $e^- - h^+$  separation. The electrochemical study of the NFs supports the proficient photocatalytic activity through  $e^-$  generation and transport. These above-said features in photocatalysts are key factors for the tremendous photocatalysis performance.

## ■ ASSOCIATED CONTENT

### ■ Supporting Information

The Supporting Information is available free of charge on the ACS Publications website at DOI: 10.1021/acs.iecr.9b00970.

Fabrication of mesoporous  $\alpha$ - $Fe_2O_3$  NFs, band gap calculation, textural properties of NFs photocatalysts, SEM of FeSiNST HNFs and FeSiNST MNPs,  $N_2$  adsorption–desorption of FeSiNST HNFs and FeSiNST MNPs, SAED of mesoporous  $TiO_2$  NFs and  $SiO_2$  NFs, STEM-EDX and UV–vis–NIR DRS spectra of NFs materials, XPS of pure  $TiO_2$ , SEM and EDX analyses of  $\alpha$ - $Fe_2O_3$  NFs, effect of pH on Cr(VI) photoreduction and 4-NP and phenol photodegradation, percent of Cr(VI) photoreduction and photodegradation, trapping experiment (PDF)

## ■ AUTHOR INFORMATION

### Corresponding Authors

\*E-mail: tu46@cornell.edu (T.U.).

\*E-mail: amaresh32@gmail.com (A.C.P.).

### ORCID

Amaresh C. Pradhan: 0000-0002-6994-3483

Tamer Uyar: 0000-0002-3989-4481

### Notes

The authors declare no competing financial interest.

## ■ ACKNOWLEDGMENTS

We are thankful to M. Guler for TEM/STEM measurement.

## ■ REFERENCES

- (1) Zhang, S.; Gao, H.; Liu, X.; Huang, Y.; Xu, X.; Alharbi, N. S.; Hayat, T.; Li, J. Hybrid 0D-2D Nanoheterostructures: In Situ Growth of Amorphous Silver Silicates Dots on g-C<sub>3</sub>N<sub>4</sub> Nanosheets for Full Spectrum Photocatalysis. *ACS Appl. Mater. Interfaces* **2016**, *8*, 35138.
- (2) Kayaci, F.; Vempati, S.; Ozgit-Akgun, C.; Donmez, I.; Biyikli, N.; Uyar, T. Transformation of polymer-ZnO core–shell nanofibers into ZnO hollow nanofibers: Intrinsic defect reorganization in ZnO and its influence on the photocatalysis. *Appl. Catal. B: Environ* **2015**, *176–177*, 646.
- (3) Pradhan, A. C.; Nanda, B.; Parida, K. M.; Rao, G. R. Fabrication of the Mesoporous Fe@MnO<sub>2</sub>NPs-MCM-41 Nanocomposite: An Efficient Photocatalyst for Rapid Degradation of Phenolic Compounds. *J. Phys. Chem. C* **2015**, *119*, 14145.
- (4) Priya, M. H.; Madras, G. Kinetics of Photocatalytic Degradation of Chlorophenol, Nitrophenol, and Their Mixtures. *Ind. Eng. Chem. Res.* **2006**, *45*, 482.
- (5) Nanda, B.; Pradhan, A. C.; Parida, K. M. Fabrication of mesoporous CuO/ZrO<sub>2</sub>-MCM-41 nanocomposites for photocatalytic reduction of Cr (VI). *Chem. Eng. J.* **2017**, *316*, 1122.
- (6) Kung, K. H.; McBride, M. B. Bonding of Chlorophenols on Iron and Aluminum Oxides. *Environ. Sci. Technol.* **1991**, *25*, 702.
- (7) Pradhan, A. C.; Sahoo, M. K.; Bellamkonda, S.; Parida, K. M.; Rao, G. R. Enhanced Photodegradation of Dyes and Mixed Dyes by Heterogeneous Mesoporous Co-Fe/Al<sub>2</sub>O<sub>3</sub>-MCM-41 Nanocomposites: Nanoparticles formation, Semiconductor Behavior and Mesoposity. *RSC Adv.* **2016**, *6*, 94263.
- (8) Kayaci, F.; Ozgit-Akgun, C.; Donmez, I.; Biyikli, N.; Uyar, T. Polymer-Inorganic Core-Shell Nanofibers by Electrospinning and Atomic Layer Deposition: Flexible Nylon-ZnO Core-Shell Nanofiber Mats and Their Photocatalytic Activity. *ACS Appl. Mater. Interfaces* **2012**, *4*, 6185.
- (9) Kayaci, F.; Vempati, S.; Ozgit-Akgun, C.; Biyikli, N.; Uyar, T. Enhanced Photocatalytic Activity of Homoassembled ZnO Nanostructures on Electrospun Polymeric Nanofibres: A Combination of Atomic Layer Deposition and Hydrothermal Growth. *Appl. Catal., B* **2014**, *156–157*, 173.
- (10) Jung, S.; Yong, K. Fabrication of CuO–ZnO nanowires on a stainless steel mesh for highly efficient photocatalytic applications. *Chem. Commun.* **2011**, *47*, 2643.
- (11) Kayaci, F.; Vempati, S.; Ozgit-Akgun, C.; Donmez, I.; Biyikli, N.; Uyar, T. Selective Isolation of Electron or Hole in Photocatalysis: ZnO-TiO<sub>2</sub> and TiO<sub>2</sub>-ZnO Core-Shell Structured Heterojunction Nanofibers via Electrospinning and Atomic Layer Deposition. *Nanoscale* **2014**, *6*, 5735.
- (12) Vinu, R.; Madras, G. Kinetics of Simultaneous Photocatalytic Degradation of Phenolic Compounds and Reduction of Metal Ions with Nano-TiO<sub>2</sub>. *Environ. Sci. Technol.* **2008**, *42*, 913.
- (13) Pradhan, A. C.; Senthamizhan, A.; Uyar, T. Electrospun Mesoporous Composite CuO–Co<sub>3</sub>O<sub>4</sub>/N-TiO<sub>2</sub> Nanofibers as Efficient Visible Light Photocatalysts. *Chem. Select.* **2017**, *2*, 7031.
- (14) Pradhan, A. C.; Uyar, T. Morphological Control of Mesoposity and Nanoparticles within Co<sub>3</sub>O<sub>4</sub>–CuO Electrospun Nanofibers: Quantum Confinement and Visible Light Photocatalysis Performance. *ACS Appl. Mater. Interfaces* **2017**, *9*, 35757.
- (15) Nie, L.; Yu, J.; Fu, J. Complete Decomposition of Formaldehyde at Room Temperature over a Platinum-Decorated Hierarchically Porous Electrospun Titania Nanofiber Mat. *Chem-CatChem* **2014**, *6*, 1983.
- (16) Abdal-hay, A.; Hamdy Makhlof, A. S.; Khalil, H. K. A. Novel, Facile, Single-Step Technique of Polymer/TiO<sub>2</sub> Nanofiber Composites Membrane for Photodegradation of Methylene Blue. *ACS Appl. Mater. Interfaces* **2015**, *7*, 13329.
- (17) Choi, S. K.; Kim, S.; Lim, S. K.; Park, H. Photocatalytic Comparison of TiO<sub>2</sub> Nanoparticles and Electrospun TiO<sub>2</sub> Nanofibers: Effects of Mesoposity and Interparticle Charge Transfer. *J. Phys. Chem. C* **2010**, *114*, 16475.
- (18) Wessel, C.; Ostermann, R.; Dersch, R.; Smarsly, B. M. Formation of Inorganic Nanofibers from Preformed TiO<sub>2</sub> Nanoparticles via Electrospinning. *J. Phys. Chem. C* **2011**, *115*, 362.
- (19) Zhan, S.; Chen, D.; Jiao, X.; Tao, C. Long TiO<sub>2</sub> Hollow Fibers with Mesoporous Walls: Sol-Gel Combined Electrospun Fabrication and Photocatalytic Properties. *J. Phys. Chem. B* **2006**, *110*, 11199.
- (20) Naik, B.; Parida, K. M.; Gopinath, C. S. Facile Synthesis of N- and S-Incorporated Nanocrystalline TiO<sub>2</sub> and Direct Solar-Light-Driven Photocatalytic Activity. *J. Phys. Chem. C* **2010**, *114*, 19473.
- (21) Asahi, R.; Morikawa, T.; Ohwaki, T.; Aoki, K.; Taga, Y. Visible-Light Photocatalysis In Nitrogen-Doped Titanium Oxides. *Science* **2001**, *293*, 269.
- (22) Khan, H.; Swati, I. K. Fe<sup>3+</sup>-doped Anatase TiO<sub>2</sub> with d–d Transition, Oxygen Vacancies and Ti<sup>3+</sup> Centers: Synthesis, Characterization, UV–vis Photocatalytic and Mechanistic Studies. *Ind. Eng. Chem. Res.* **2016**, *55*, 6619.
- (23) Nakamura, R.; Okamoto, A.; Osawa, H.; Irie, H.; Hashimoto, K. Design of All-Inorganic Molecular-Based Photocatalysts Sensitive to Visible Light: Ti (IV)-O-Ce (III) Bimetallic Assemblies on Mesoporous Silica. *J. Am. Chem. Soc.* **2007**, *129*, 9596.
- (24) Pradhan, A. C.; Martha, S.; Mahanta, S. K.; Parida, K. M. Mesoporous nanocomposite Fe/Al<sub>2</sub>O<sub>3</sub>-MCM-41: An efficient photocatalyst for hydrogen production under visible light. *Int. J. Hydrogen Energy* **2011**, *36*, 12753.
- (25) Sing, K. S. W.; Everett, D. H.; Haul, R. A. W.; Moscou, L.; Pierotti, R. A.; Rouquerol, J.; Siemieniewska, T. Reporting Physisorption Data for Gas/Solid Systems with Special Reference to the Determination of Surface area and Porosity. *Pure Appl. Chem.* **1985**, *57*, 603.

- (26) Ji, X.; Lee, K. T.; Nazar, L. F. A Highly Ordered Nanostructured Carbon–Sulphur Cathode for Lithium–Sulphur Batteries. *Nat. Mater.* **2009**, *8*, 500.
- (27) Pal, M.; Rakshit, R.; Mandal, K. Facile Functionalization of Fe<sub>2</sub>O<sub>3</sub> Nanoparticles to Induce Inherent Photoluminescence and Excellent Photocatalytic Activity. *Appl. Phys. Lett.* **2014**, *104*, 233110.
- (28) Lopez, R.; Gomez, R. Band-gap Energy Estimation from Diffuse Reflectance Measurements on Sol–Gel and Commercial TiO<sub>2</sub>: A Comparative Study. *J. Sol-Gel Sci. Technol.* **2012**, *61*, 1.
- (29) Naldoni, A.; Allietta, M.; Santangelo, S.; Marelli, M.; Fabbri, F.; Cappelli, S.; Bianchi, C. L.; Psaro, R.; Dal Santo, V. Effect of Nature and Location of Defects on Bandgap Narrowing in Black TiO<sub>2</sub> Nanoparticles. *J. Am. Chem. Soc.* **2012**, *134*, 7600.
- (30) Wang, X.; Yan, Y.; Hao, B.; Chen, G. Biomimetic layer-by-layer deposition assisted synthesis of Cu, N co-doped TiO<sub>2</sub> nanosheets with enhanced visible light photocatalytic performance. *Dalton Trans.* **2014**, *43*, 14054.
- (31) Wang, E.; He, T.; Zhao, L.; Chen, Y.; Cao, Y. Improved visible light photocatalytic activity of titania doped with tin and nitrogen. *J. Mater. Chem.* **2011**, *21*, 144.
- (32) Dhlaminia, M. S.; Terblansa, J. J.; Kroona, R. E.; Ntwaeaborwaa, O. M.; Ngaruiyaa, J. M.; Bothab, J. R.; Swarta, H. C. Photoluminescence properties of SiO<sub>2</sub> surface-passivated PbS nanoparticles. *S. Afr. J. Sci.* **2008**, *104*, 398.
- (33) Liu, K.; Su, C.-Y.; Perng, T.-P. Highly porous N-doped TiO<sub>2</sub> hollow fibers with internal three-dimensional interconnected nanotubes for photocatalytic hydrogen production. *RSC Adv.* **2015**, *5*, 88367.
- (34) Lim, S. P.; Pandikumar, A.; Huang, N. M.; Lim, H. N.; Gu, G.; Ma, T. L. Promotional effect of silver nanoparticles on the performance of N-doped TiO<sub>2</sub> photoanode-based dye-sensitized solar cells. *RSC Adv.* **2014**, *4*, 48236.
- (35) Marcus, R. Chemical and Electrochemical Electron-Transfer Theory. *Annu. Rev. Phys. Chem.* **1964**, *15*, 155.
- (36) Li, Y.; Wang, Z.; Lv, X.-J. N-Doped TiO<sub>2</sub> Nanotubes/N-doped Graphene Nanosheets Composites as High Performance Anode Materials in Lithium-Ion Battery. *J. Mater. Chem. A* **2014**, *2*, 15473.
- (37) Rodriguez, J. A.; Jirsak, T.; Dvorak, J.; Sambasivan, S.; Fischer, D. J. Reaction of NO<sub>2</sub> with Zn and ZnO: Photoemission, XANES, and Density Functional Studies on the Formation of NO<sub>3</sub>. *J. Phys. Chem. B* **2000**, *104*, 319.
- (38) Fang, J.; Liu, W.; Yu, F.; Qin, F.; Wang, M.; Zhang, K.; Lai, Y. Fe, S Co-Doped Anatase TiO<sub>2</sub> Nanotubes as Anodes with Improved Electrochemical Performance for Lithium Ion Batteries. *RSC Adv.* **2016**, *6*, 70133.
- (39) Ohno, T.; Akiyoshi, M.; Umeyashiki, T.; Asai, K.; Mitsui, T.; Matsumura, M. Preparation of S-Doped TiO<sub>2</sub> Photocatalysts and their Photocatalytic Activities Under Visible Light. *Appl. Catal., A* **2004**, *265*, 115.
- (40) Seetharaman, A.; Sivasubramanian, D.; Gandhiraj, V.; Soma, V. R. Tunable Nanosecond and Femtosecond Nonlinear Optical Properties of C-N-S-Doped TiO<sub>2</sub> Nanoparticles. *J. Phys. Chem. C* **2017**, *121*, 24192.
- (41) Morgan, W. E.; Van Wazer, J. R. Binding Energy Shifts in the X-Ray Photoelectron Spectra of a Series of Related Group IV-a Compounds. *J. Phys. Chem. C* **1973**, *77*, 964.
- (42) Pham, M.-H.; Dinh, C.-T.; Vuong, G.-T.; Ta, N.-D.; Do, T.-O. Visible Light Induced Hydrogen Generation Using A Hollow Photocatalyst with Two Cocatalysts Separated on Two Surface Sides. *Phys. Chem. Chem. Phys.* **2014**, *16*, 5937.
- (43) Bakar, S. A.; Byzinski, G.; Ribeiro, C. Synergistic effect on the photocatalytic activity of N-doped TiO<sub>2</sub> nanorods synthesised by novel route with exposed (110) facet. *J. Alloys Compd.* **2016**, *666*, 38.
- (44) Bharti, B.; Kumar, S.; Lee, H.-N.; Kumar, R. Formation of Oxygen Vacancies and Ti<sup>3+</sup> State in TiO<sub>2</sub> Thin Film and Enhanced Optical Properties by Air Plasma Treatment. *Sci. Rep.* **2016**, *6*, 32355.
- (45) Liu, G. J.; Ye, S.; Yan, P. L.; Xiong, F. G.; Fu, P.; Wang, Z. L.; Chen, Z.; Shi, J. Y.; Li, C. Enabling an Integrated Tantalum Nitride Photoanode to Approach the Theoretical Photocurrent Limit for Solar Water Splitting. *Energy Environ. Sci.* **2016**, *9*, 1327.
- (46) Srivastav, A.; Verma, A.; Banerjee, A.; Khan, S. A.; Gupta, M.; Satsangi, V. R.; Shrivastav, R.; Dass, S. Gradient doping—a case study with Ti–Fe<sub>2</sub>O<sub>3</sub> towards an improved photoelectrochemical response. *Phys. Chem. Chem. Phys.* **2016**, *18*, 32735.
- (47) Shen, S.; Zhou, J.; Dong, C.-L.; Hu, Y.; Tseng, E. N.; Guo, P.; Guo, L.; Mao, S. S. Surface Engineered Doping of Hematite Nanorod Arrays for Improved Photoelectrochemical Water Splitting. *Sci. Rep.* **2014**, *4*, 6627.
- (48) Meng, X. Y.; Qin, G. W.; Li, S.; Wen, X. H.; Ren, Y. P.; Pei, W. L.; Zuo, L. Enhanced photoelectrochemical activity for Cu and Ti doped hematite: The first principles calculations. *Appl. Phys. Lett.* **2011**, *98*, 112104.
- (49) Yang, Y.; Xu, D.; Wu, Q.; Diao, P. Cu<sub>2</sub>O/CuO Bilayered Composite as a High-Efficiency Photocathode for Photoelectrochemical Hydrogen Evolution Reaction. *Sci. Rep.* **2016**, *6*, 35158.
- (50) Kandi, D.; Martha, S.; Thirumurugan, A.; Parida, K. M. Modification of BiOI Microplates with CdS QDs for Enhancing Stability, Optical Property, Electronic Behavior toward Rhodamine B Decolorization, and Photocatalytic Hydrogen Evolution. *J. Phys. Chem. C* **2017**, *121*, 4834.
- (51) Hou, H.; Wang, L.; Gao, F.; Wei, G.; Tang, B.; Yang, W.; Wu, T. General Strategy for Fabricating Thoroughly Mesoporous Nanofibers. *J. Am. Chem. Soc.* **2014**, *136*, 16716.
- (52) Dong, W.; Yen, S.-P.; Paik, J.-A.; Sakamoto, J. The Role of Acetic Acid and Glycerol in the Synthesis of Amorphous MgO Aerogels. *J. Am. Ceram. Soc.* **2009**, *92*, 1011.
- (53) Zhang, Y.; Dai, R.; Hu, S. Study of the role of oxygen vacancies as active sites in reduced graphene oxide-modified TiO<sub>2</sub>. *Phys. Chem. Chem. Phys.* **2017**, *19*, 7307.
- (54) Yan, L. G.; Yang, K.; Shan, R. R.; Yu, H. Q.; Du, B. Calcined ZnAl- and Fe<sub>3</sub>O<sub>4</sub>/ZnAl-layered double hydroxides for efficient removal of Cr(VI) from aqueous solution. *RSC Adv.* **2015**, *5*, 96495.
- (55) Jabeen, H.; Chandra, V.; Jung, S.; Lee, J. W.; Kim, K. S.; Kim, S. B. Enhanced Cr (VI) removal using iron nanoparticle decorated grapheme. *Nanoscale* **2011**, *3*, 3583.